

Final Report for AOARD Grant FA2386-12-1-4068  
**“Growth of GaN- and ZnO-based Nanorod Compound Structures”**

**August 16, 2013**

**Name of Principal Investigators:** Chih-Chung (C. C.) Yang

- e-mail address : ccy@cc.ee.ntu.edu.tw
- Institution : Graduate Institute of Photonics and Optoelectronics, National Taiwan University
- Mailing Address : No. 1, Roosevelt Road, Section 4, Taipei, 10617 Taiwan
- Phone : +886-2-23657624
- Fax : +886-2-23652637

Period of Performance: 06/01/2012 – 05/31/2013

**Abstract:**

The cross-sectional sizes of the regularly-patterned GaN nanorods (NRs) and InGaN/GaN quantum-well (QW) NRs of different heights and different hexagon orientations, which are grown on the patterned templates of different hole diameters, pitches, and crystal orientations, are compared. It is found that the cross-sectional size of the GaN NR, which is formed with the pulsed growth mode, is mainly controlled by the patterned hole diameter, and the thickness of the sidewall QW structure is mainly determined by the NR height. The cross-sectional size variation of GaN NR is interpreted by the quasi-three-dimensional nature of atom supply amount for precipitating a two-dimensional disk-shaped NR segment. The variation of the sidewall QW structure is explained by the condition of constituent atom supply in the gap volume between the neighboring NRs. Also, we compare the cathodoluminescence emission wavelengths among those samples of different growth conditions. Generally speaking, the QW NR with a smaller height, a larger cross-sectional size, or a larger pitch has a longer emission wavelength. Also, the void structures and related optical properties after thermal annealing with ambient oxygen in regularly patterned ZnO NR arrays grown with the hydrothermal method are studied. In increasing the thermal annealing temperature, based on the transmission electron microscopy and backscattering electron microscopy observations, void distribution starts from the bottom and extends to the top of an NR in the vertical (c-axis) growth region. When the annealing temperature becomes higher than 400 °C, void distribution spreads into the lateral (m-axis) growth region. Photoluminescence measurement shows that the n-ZnO band-edge emission, in contrast to defect emission in the yellow-red range, is the strongest under the n-ZnO NR process conditions of 0.08 M in growth solution concentration, 0.003 M in Ga doping concentration, 80 °C in growth temperature, 180 min in growth duration, and 300 °C in thermal annealing temperature with ambient oxygen for 60 min. Energy dispersive X-ray spectroscopy data indicate that the concentration of hydroxyl groups, which take the positions of anions in ZnO, in the vertical-growth region is

Report Documentation Page				Form Approved OMB No. 0704-0188	
Public reporting burden for the collection of information is estimated to average 1 hour per response, including the time for reviewing instructions, searching existing data sources, gathering and maintaining the data needed, and completing and reviewing the collection of information. Send comments regarding this burden estimate or any other aspect of this collection of information, including suggestions for reducing this burden, to Washington Headquarters Services, Directorate for Information Operations and Reports, 1215 Jefferson Davis Highway, Suite 1204, Arlington VA 22202-4302. Respondents should be aware that notwithstanding any other provision of law, no person shall be subject to a penalty for failing to comply with a collection of information if it does not display a currently valid OMB control number.					
1. REPORT DATE <b>13 DEC 2013</b>		2. REPORT TYPE <b>Final</b>		3. DATES COVERED <b>01-12-2011 to 01-12-2012</b>	
4. TITLE AND SUBTITLE <b>Growth of Gallium Nitride and Zinc Oxide Nanorod Compound Structures</b>				5a. CONTRACT NUMBER <b>FA23861214068</b>	
				5b. GRANT NUMBER	
				5c. PROGRAM ELEMENT NUMBER	
6. AUTHOR(S) <b>Chih-Chung Yang</b>				5d. PROJECT NUMBER	
				5e. TASK NUMBER	
				5f. WORK UNIT NUMBER	
7. PERFORMING ORGANIZATION NAME(S) AND ADDRESS(ES) <b>National Taiwan University, No. 1, Section 4, Roosevelt Raod,, Taipei 10617, Taiwan, TW, 10617</b>				8. PERFORMING ORGANIZATION REPORT NUMBER <b>N/A</b>	
9. SPONSORING/MONITORING AGENCY NAME(S) AND ADDRESS(ES) <b>AOARD, UNIT 45002, APO, AP, 96338-5002</b>				10. SPONSOR/MONITOR'S ACRONYM(S) <b>AOARD</b>	
				11. SPONSOR/MONITOR'S REPORT NUMBER(S) <b>AOARD-124068</b>	
12. DISTRIBUTION/AVAILABILITY STATEMENT <b>Approved for public release; distribution unlimited</b>					
13. SUPPLEMENTARY NOTES					
14. ABSTRACT <b>The cross-sectional sizes of the regularly-patterned GaN nanorods (NRs) and InGa<sub>N</sub>/Ga<sub>N</sub> quantum-well (QW) NRs of different heights and different hexagon orientations, which are grown on the patterned templates of different hole diameters, pitches, and crystal orientations, are compared. It is found that the cross-sectional size of the GaN NR, which is formed with the pulsed growth mode, is mainly controlled by the patterned hole diameter, and the thickness of the sidewall QW structure is mainly determined by the NR height. The cross-sectional size variation of GaN NR is interpreted by the quasi-three-dimensional nature of atom supply amount for precipitating a two-dimensional disk-shaped NR segment. The variation of the sidewall QW structure is explained by the condition of constituent atom supply in the gap volume between the neighboring NRs.</b>					
15. SUBJECT TERMS <b>Gallium Nitride , nano materials, Detector Technology, Electronic Devices, Coalescence Overgrowth, Threading Dislocations</b>					
16. SECURITY CLASSIFICATION OF:			17. LIMITATION OF ABSTRACT <b>Same as Report (SAR)</b>	18. NUMBER OF PAGES <b>34</b>	19a. NAME OF RESPONSIBLE PERSON
a. REPORT <b>unclassified</b>	b. ABSTRACT <b>unclassified</b>	c. THIS PAGE <b>unclassified</b>			



significantly higher than that in the lateral-growth region of an NR. During thermal annealing, hydroxyl groups are desorbed from the NR leaving anion vacancies for reacting with cation vacancies to form void cores. The thermal energy provides energy for merging small voids into large ones.

**Table of Contents:**

Part I: Cross-sectional sizes and emission wavelengths of regularly patterned GaN and core-shell InGaN/GaN quantum-well nanorod arrays .....p. 3

Part II: Regularly patterned ZnO nanorods grown with the hydrothermal method .....p. 20

Part III: Related Journal Publication List (acknowledging AOARD) .....p. 33

## Part I:

# Cross-sectional sizes and emission wavelengths of regularly patterned GaN and core-shell InGaN/GaN quantum-well nanorod arrays

## 1. Introduction

Due to the advantages of high crystal quality,<sup>1,2</sup> larger emission volume,<sup>3,4</sup> non-polar and semi-polar quantum well (QW) growths,<sup>5-12</sup> increased indium incorporation,<sup>13-16</sup> enhanced light extraction,<sup>17</sup> and coalesced growth of high crystal quality,<sup>18,19</sup> the fabrication of InGaN/GaN QW nanorod (NR) light-emitting diode (LED) arrays has attracted much research attention. Although the growth of randomly distributed nitride NRs can provide us with certain physical insides of NR structure and emission property,<sup>7,20-24</sup> regularly patterned NR arrays based on selective growth are more useful from a practical point of view. Patterned growth of NR LED structures have been grown with metalorganic chemical vapor deposition (MOCVD).<sup>25,26</sup> Although continuous growth can also lead to the formation of a quasi-regularly patterned nitride NR or micro-rod array,<sup>27-32</sup> regularly patterned nitride NR arrays of high uniformity are usually formed with pulsed MOCVD growth, which is based on the self-catalytic growth of the vapor-liquid-solid (VLS) mode.<sup>1,18,33</sup> In this growth method, the sources of Ga and N are switched on and off alternatively with a growth pause in between for forming GaN NR arrays. To form an InGaN/GaN QW LED structure, n-type GaN NRs can be first grown along the c-axis based on the aforementioned pulsed growth method. Then, with the ordinary two-dimensional (2-D) growth mode, the QW structures can be deposited onto the top face to form the polar QWs and the hexagonal sidewalls (*m*-plane) to form non-polar QWs. If the {1-101} slant facets are formed in the n-GaN NRs, semi-polar QWs on such a facet can also be deposited.

In fabricating such an NR LED array, the cross-sectional size, height, and the NR spacing need to be carefully controlled for optimizing the LED fabrication process and the resultant performances. To increase the sidewall emission area, both the NR height and planar NR density must be large. However, in this situation, the LED process becomes difficult, particularly when a dielectric material needs to be inserted into the gaps between NRs. Also, although a larger NR cross-sectional size can provide us with a larger sidewall area for increasing the emission volume, the crystal quality can become lower and the strain relaxation effect in such an NR can be weakened. Meanwhile, the smaller gaps between NRs result in LED fabrication difficulty. Therefore, the diameter and pitch of the patterned holes on a template for NR growth and the grown NR height need to be well designed for optimizing the LED performances. Before such a design can be implemented, we need to understand the relations between the cross-sectional size and height of the NRs and the patterned hole diameter and pitch.

In this paper, we study the dependencies of the cross-sectional sizes of the regularly-patterned GaN NRs, which are grown based on the pulsed MOCVD growth method, and InGaN/GaN QW NRs with different heights and different hexagon orientations on the hole diameter, pitch, and crystal orientation of the patterned template. It is found that the cross-sectional size of the GaN NR is mainly controlled

by the patterned hole diameter and is weakly dependent on the NR height, pitch, and pattern orientation. Also, the thickness of the sidewall QW structure is mainly determined by the NR height and is weakly affected by the patterned hole diameter, pitch, and pattern orientation. Meanwhile, we compare the cathodoluminescence (CL) emission wavelengths among different samples to show that the emission wavelength is related to the NR height, cross-sectional size, pitch of the pattern, and pattern orientation. In section 2 of this paper, the NR sample growth procedures and the measurement conditions are presented. The results of scanning electron microscopy (SEM) and transmission electron microscopy (TEM) observations are shown in section 3. Then, in section 4, the CL measurement results are reported. Discussions are given in section 5. Finally, conclusions are drawn in section 6.

## 2. Sample Preparation Procedures and Measurement Conditions

To understand the dependencies of NR cross-sectional size and QW emission wavelength on the hole pattern parameters, we prepare three triangular hole patterns on GaN templates with SiO<sub>2</sub> masks through the nano-imprint lithography technique. The three hole patterns are denoted by 250/700, 180/500, and 180/400. The first and second numbers in nm for each pattern represent the hole diameter and pitch (the center-to-center distance between two nearest neighboring holes), respectively. Based on the three hole patterns, GaN NRs are grown using the pulsed growth technique. Six samples (samples I-VI) of different InGaN/GaN NR structures are prepared for comparison with their sample parameters listed in Table I and the preparation procedures described below.

The NR growth is patterned with the nano-imprint technique on a 2-  $\mu$ m-thick GaN template, which is deposited with MOCVD on *c*-plane sapphire substrate.<sup>1,18</sup> On the wafer, 2-D triangular patterns of circular holes of different parameters mentioned in the last paragraph are formed on a 40-nm-thick SiO<sub>2</sub> mask. Figures 1(a) and 1(b) show the plan-view (with 5 kV in electron acceleration voltage) and 30°-tilted scanning electron microscopy (SEM) images, respectively, of the 250/700 hole pattern. From the plan-view image, one can see that the holes are essentially circular in shape. The growth of GaN NRs starts with a hole-filling process under the MOCVD conditions of 100 torr in chamber pressure, 1500 rpm in turbo disc speed, 1050 °C in substrate temperature, 50 sccm in TMGa flow rate, 1500 sccm in NH<sub>3</sub> flow rate (1100 in V/III ratio), and 12 sec in growth duration. After the hole filling process, the pulsed MOCVD growth mode is used at 1050 °C with V/III ratio at 550 for forming flat-top GaN NRs of a hexagonal cross-sectional shape.<sup>1,18,33</sup> In this process, TMGa (50 sccm) and NH<sub>3</sub> (500 sccm) flows are switched on and off alternatively with the flow durations of TMGa and NH<sub>3</sub> at 20 and 30 sec, respectively. A pause of 0.5 sec in duration is applied after each TMGa flow cycle. After the pulsed growth for 37 cycles (~31 min in duration), regularly patterned GaN NRs of uniform geometry with a height of ~1000 nm are obtained. The NR height is proportional to the growth cycle number and is weakly dependent on the patterned hole diameter and pitch. In other words, in all the hole patterns, the increment of NR height in a growth cycle is a constant (~27 nm). Therefore, with 18 pulsed growth cycles, a GaN NR array of ~500 nm in height is obtained. On the GaN NRs, three periods of InGaN/GaN QWs are deposited with the conventional 2-D MOCVD growth mode under the conditions of 200 torr in chamber pressure, 750 rpm in turbo

disc speed, 32 sccm in TEGa flow rate, 2700 sccm in  $\text{NH}_3$  flow rate, and 240 sccm in TMIn flow rate (only applied to the growth of the InGaN well layers). The growth temperature and duration of the InGaN well (GaN barrier) in the QW structures are 700 °C and 1.25 min (870 °C and 11 min), respectively.

It is noted that in the nano-imprint process, the hole pattern can be arranged to align its hexagonal *m*-axis (the orientation along a nearest-hole sequence) to be perpendicular to or parallel with the *a*-axis of sapphire crystal. With these two pattern arrangements, we can obtain two different planar orientations of the hexagonal NRs. When the *m*-axis of the hole pattern is perpendicular to the *a*-axis of sapphire crystal that will be referred to as the side-by-side pattern, the line connecting the centers of the two nearest neighboring NRs crosses perpendicularly the two parallel lateral sides of individual NRs. When the *m*-axis of the hole pattern is parallel with the *a*-axis of sapphire crystal that will be referred to as the edge-to-edge pattern, the line connecting the centers of the two nearest neighboring NRs is either parallel with or forming a 60° tilted angle with respect to the two parallel lateral sides of individual NRs. In the edge-to-edge pattern, the shortest distance between the two nearest NRs corresponds to one of the edges of individual NRs.

As shown in rows 1-4 of Table I, samples I-IV have the side-by-side NR orientation and samples V and VI have the edge-to-edge NR orientation. Samples I and IV are prepared based on the 250/700 hole pattern. However, they have different NR heights. Samples II and V (III and VI) are prepared based on the 180/500 (180/400) hole pattern. Except sample IV, which has the NR height at ~500 nm, all the samples have the NR height at ~1000 nm.

The SEM measurement is performed with a JEOL JSM-7001F system, in which a Gatan MonoCL4 module is installed for CL measurement. The SEM results are obtained with the operation conditions of 15 kV in acceleration voltage unless otherwise specified, 0.3 nA in probe current, and ~3 nm in spatial resolution. Two acceleration voltages of 5 and 15 kV are used in CL measurements with 7 nA in probe current and ~10 nm in spatial resolution. A local CL spectral measurement covers a spatial domain of 100 x 75 nm<sup>2</sup> in dimension. The TEM investigation is performed using a Philips Tecnai F30 field-emission electron microscope with an accelerating voltage of 300 kV and a probe forming lens of Cs = 1.2 mm.

### 3. SEM and TEM Observations

Figures 2(a)-2(f) show the plan-view SEM images of samples I-VI, respectively. Here, one can see that the cross sections of most NRs are hexagonal in shape of high symmetry. Although the central portion of the top face in any of the six NR samples is flat, tilted facets exist at the edge of the top face of a GaN NR. However, because the areas of the tilted facets are small, it is difficult to observe them in the SEM images. The comparison between Figs. 2(b) and 2(e) or between Figs. 2(c) and 2(f) demonstrates the different hexagon orientations between the side-by-side and edge-to-edge patterns. Figures 2(g) and 2(h) show the 30°-tilted SEM images of samples I and IV, respectively. Here, the different NR heights of the two samples can be seen. The cross-sectional size of a GaN NR, which is defined as the distance between two parallel lateral sides, of each sample is listed in row 5 of Table I. Also, the cross-sectional size increment, which is defined as the difference between the NR cross-sectional size and the hole diameter of the growth template, of

each sample is given in row 6 of the same table. Here, one can see that the GaN NR cross-sectional size is only dependent on the hole diameter of the growth template. When the hole diameter is 250 (180) nm, the GaN NR cross-sectional size is around 376 (243) nm. The small deviation of sample V (only by 4 nm) can be attributed to the slight NR size fluctuation across the wafer. The cross-sectional size is independent of the grown NR height and the pitch of the template pattern. It is noted that the small-area tilted facets at the edge of the NR top can be seen in Fig. 2(g) or 2(h).

Figure 3 shows the cross-sectional high angle annular dark field (HAADF) image in TEM observation of an InGaN/GaN QW NR of sample I. In this image, the three almost vertical bright lines (indicated by short arrows) near the sidewall on the right-hand side correspond to the three QWs. The sidewall QW structure will be discussed in detail with other TEM images later. Here, we focus on the pulsed growth result of a GaN NR. The (greenish) long-dashed lines indicate the boundary of the GaN NR. A quasi-periodic bright line pattern (horizontal in the central portion) in the image portion of the GaN NR can be clearly seen to show the pulsed growth process. The line pattern shown in the HAADF image is formed between the successive precipitation stages in pulsed growth. The physical causes for such a line pattern deserves further investigation. The two horizontal continuous (blue) lines are drawn along the line pattern to indicate the thickness of a pulsed-growth period (~27 nm). Between the vertical (greenish) long-dashed line on the right and the vertical (pink) short-dashed line, the image line pattern becomes tilted, as indicated by the three slant continuous (red) lines. Figure 3 clearly illustrates not only the pulsed growth process, but also the tilted facets at the edge of the top of a GaN NR. In other words, a GaN NR has a truncated pyramidal top face. However, in most growth results of ours, the areas of the tilted facets are quite small and cannot be easily observed in a plan-view or cross-sectional SEM image.

Figures 4(a) and 4(b) (4(c) and 4(d)) show the plan-view (30°-tilted) SEM images with two different scales of sample I after three periods of InGaN/GaN QW are deposited on the top face and sidewalls to form QW NRs. Here, one can see that after the growth of the QW structure, the shape of the NR top becomes truncated pyramidal with tilted facets of large areas. Figures 4(e) and 4(f) show the plan-view SEM images of the QW NRs of samples II and III, respectively. Here, the flat area in the truncated pyramidal structure at the NR top becomes quite small. Figures 4(g) and 4(h) show the plan-view and 30°-tilted SEM images of the QW NRs of sample IV. They also show the truncated pyramids at the NR tops. Then, Figs. 5(a) and 5(b) (Figs. 5(c) and 5(d)) show the plan-view and 30°-tilted SEM images of the QW NRs of sample V (VI), respectively. From Figs. 4 and 5, one can see that the cross-sectional sizes of the NRs become larger after the QW structures are deposited. Also, the almost pointed pyramidal tops are formed in the QW NRs grown on the templates of the smaller hole diameter (180 nm), and the truncated pyramidal tops are formed in those grown on the templates of the larger hole diameter (250 nm).

The cross-sectional sizes of the QW NRs of various samples are listed in row 7 of Table I. The thickness value of the sidewall QW structure of the QW NRs, which is defined as one-half the difference between the cross-sectional sizes before and after the growth of the QW structure (the difference between rows 5 and 7 in Table I), of each sample is shown in row 8 of Table I. Here, we can see that the thickness



values of the sidewall QW structure in different samples can be roughly classified into two groups: 40.5 nm of sample VI (short NRs) and 23-27.5 nm of all other samples (tall NRs). From this result, we can conclude that the sidewall-growth thickness of the three-period QW structure is mainly controlled by the NR height and is weakly dependent on the cross-sectional size and pitch of the original GaN NR. A shorter GaN NR leads to a thicker sidewall growth. Meanwhile, the sidewall-growth thickness of the edge-to-edge pattern is slightly smaller than that of the side-by-side pattern.

Figures 6(a)-6(e) show the TEM images of a QW NR of sample I. In all the images, the QWs are indicated by arrows. In Fig. 6(a), one can see the three top-face QWs and the three sidewall QWs on each side of the NR. Figures 6(b)-6(d) show the magnified images around the top, the sidewall near the top, and the sidewall near the bottom (not shown in Fig. 6(a)), respectively. The sidewall QWs look narrower, when compared with the top-face QWs.<sup>8</sup> Figure 6(e) shows that on the slant facet (the (1-101) plane), any well-shaped QW structure can hardly be observed. Figures 7(a)-7(c) show the TEM images of a QW NR, which fell during TEM specimen preparation. Here, one can observe the cross-sectional structure of the NR. In Fig. 7(a), we can see the three QWs on each of the six lateral sides. Clearer QW structures can be seen in the magnified images of Figs. 7(b) and 7(c). Figures 6 and 7 provide us with the strong evidences for the growths of the top-face c-plane and sidewall m-plane QWs.

#### 4. CL Measurement Results

Figures 8(a) and 8(b) (8(c) and 8(d)) show the plan-view CL mapping images with the panchromatic spectrum and the emission wavelength at 444 nm, respectively, of sample I when the electron acceleration voltage in CL measurement is 5 (15) kV. The wavelength of 444 nm corresponds to the spectral peak of the plan-view CL measurement in a large scale of sample I. The corresponding CL mapping images of sample IV look similar to those in Figs. 8(a)-8(d). In Figs. 8(a)-8(d), every image shows a brighter rim belt pattern, indicating the strong emission from the sidewall QW structure due to its larger emission volume as the excitation electrons penetrate into the sample along the sidewall. Figures 9(b) and 9(c) (9(e) and 9(f)) show the cross-sectional panchromatic CL mapping images of sample I (IV) at the same location as the cross-sectional SEM image shown in Fig. 9(a) (9(d)), which is taken at 5 kV in electron acceleration voltage, when the electron acceleration voltage in CL measurement is 5 and 15 kV, respectively. The bright sidewall QW emission can also be seen in Figs. 9(c) and 9(f), as indicated by the short arrows.

The line-scan intensity profiles along the double-headed arrows shown in Figs. 8(a), 8(c), 9(b), and 9(c) for sample I are plotted as the four curves in Fig. 10, in which the letters “P” and “C” refer to the plan-view and cross-sectional observations, respectively. Here, one can see the almost flat intensity distributions across the NR cross section in the case of 15 kV in electron acceleration voltage (curve P-15kV) while the two peaks at the two rims of the NRs are quite clear in the case of 5 kV (curve P-5kV). It is noted that the two edges (central portion) of the line-scan intensity profiles in the upper two curves of Fig. 10 originate from the emission of the sidewall (top-face) QWs. The different line-scan results between the cases of 5 and 15 kV are attributed to the different electron penetration depths. In the case of 5

kV, the electron penetration is shallower such that not all the three top-face QWs are fully excited and their emission is relative weaker, when compared with the case of 15 kV. In the lower two curves (curves C-5kV and C-15kV), the two peaks at the edges in the line-scan profiles are more prominent in the case of 15 kV, when compared with the case of 5 kV. This is so because in the cross-sectional CL excitation, when electron penetration is shallow, the emission is mainly from the QWs on the proximate sidewall facets such that the intensity at the central portion of the line-scan profile can be comparable to those at the two edges. However, when electron penetration is deep in the case of 15 kV, more QW regions on other sidewall facets can be excited such that the emission intensity at the two edges becomes significantly stronger for showing the clear peaks at the edges. It is noted that the corresponding line-scan CL intensity profiles for sample IV are similar to those for sample I.

Figure 11 shows the CL spectra of sample I measured at different locations and different view directions, including that from the large-scale plan-view (PV) measurement, that at the center on the top face of an NR (PV-c), that at the rim on the top face of the NR (PV-r), that from the large-scale cross-sectional (CS) measurement, that at a point near the top of the sidewall of an NR (CS-t), near the middle height of the sidewall of the NR (CS-m), and near the bottom of the sidewall of the NR (CS-b). For comparison, the plan-view CL spectrum of the bare GaN NR array is also plotted as curve PV-GaN. All the CL spectra are obtained by using the electron acceleration voltage of 5 kV. The positions for local CL spectral measurements are marked by the squares on the top face, as shown in Fig. 8(a), and by the crosses on the sidewall, as shown in Fig. 9(a). The strong defect emission in the spectral range beyond 480 nm in the bare GaN NRs due to the effective excitation of defect emission in CL measurement can be seen. Basically, except the variation of CL spectrum between different sidewall heights, the QW emission spectral peaks are all around 440 nm in sample I. The corresponding CL spectra of sample IV are similar to those of sample I except that the peak wavelength is shifted to ~450 nm. The spectral peaks of those curves in Fig. 11 and the corresponding results of sample IV are listed in columns 2 and 5 of Table II, respectively. The QWs on sample IV of shorter NRs emit longer-wavelength light, when compared with those on sample I of longer NRs. The CL spectral peaks under the plan-view measurement condition, including the local and large-scale measurements, of samples II, III, V, and VI are listed in columns 3, 4, 6, and 7, respectively, of Table II. Generally speaking, the CL spectral peak wavelengths of samples I and IV are longer than those of samples II and III, followed by those of samples V and VI. Detailed discussions will be given in the next section.

## 5. Discussions

To interpret the cross-sectional size variations of NRs shown in Table I, we propose a model with the self-catalytic VLS growth scenario schematically shown in Fig. 12(a). Here, a sphere-like Ga droplet is formed on the top of a hexagonal GaN NR representing the condition at the end of the first-half cycle of pulsed growth, during which only Ga source is supplied. The disk-like layer of a truncated pyramidal shape, represented by the greener region at the top of the GaN NR, is drawn to stand for the precipitated layer in one cycle of pulsed growth. The similar experimental

condition is shown in Fig. 12(b). This 30°-tilted SEM image is taken from a sample, on which the growth stops at the end of the first half-cycle of Ga source supply in pulsed growth. As shown in Fig. 12(a),  $d$  is the diameter of the sphere-like Ga droplet and  $a$  is roughly the cross-sectional size of the NR. Suppose that the hole diameter of the template is  $b$ . It is reasonable to assume that  $d$  is approximately equal to  $b$  because at the beginning of pulsed growth, i.e., when an NR just emerges from the filled hole, the GaN droplet size must be about the same as the hole diameter due to the nature of selective growth. Therefore, it is reasonable to assume  $d \sim b$ . Assume that the increment of NR height in each pulsed growth cycle is  $t$ , which is supposed to be a constant, independent of the patterned hole diameter. The total amount of atoms in the disk volume precipitated in each growth cycle is  $3^{1/2} a^2 t/2$ , where  $\alpha$  is assumed to be the atomic density in the GaN NR. This amount of atoms is supplied by the super-saturated volume of  $\sim \beta(4/3)\pi(d/2)^3 = \beta\pi d^3/6 \sim \beta\pi b^3/6$  in the catalytic Ga droplet. Here,  $\beta$  is the atomic density in the catalytic Ga droplet. Therefore, we have  $3^{1/2} \alpha a^2 t/2 \sim \beta\pi b^3/6$ . In other words, if we use two hole diameters  $b_1$  and  $b_2$  to grow NRs for obtaining the NR cross-sectional sizes  $a_1$  and  $a_2$ , respectively, we can obtain the approximated relationship as

$$\frac{a_1}{a_2} \approx \left( \frac{b_1}{b_2} \right)^{3/2}. \quad (1)$$

Hence, by setting  $b_1 = 250$  nm and  $b_2 = 180$  nm, we have the cross-sectional size ratio of GaN NR between samples I and II as  $(250/180)^{3/2} = 1.64$  based on the proposed model. In experiment, from Table I, the corresponding ratio is  $376/242 = 1.55$ , which reasonably agrees with the model value of 1.64. Based on the proposed model, we can see that the cross-sectional size of GaN NR is essentially controlled by the patterned hole diameter.

For growing the QW structures, the MOCVD growth is switched to the ordinary 2-D growth mode. In this situation, we use a growth model, which was introduced for interpreting the nanowire growth with molecular beam epitaxy,<sup>34,35</sup> to give a qualitative explanation for the results shown in Table II. In this model, when the supplied atoms are coming down from above toward the substrate and fall into the regions of NR cross section, they are used for growing the QW structure on the NR top face. On the other hand, when the supplied atoms fall into the regions of the gaps between the NRs, they fall down to the bottom of the gaps and migrate upward along the NR sidewalls if the substrate temperature is high enough. Part of those atoms is attached to the sidewalls for forming the sidewall QW structure. The other part of those atoms, which are not used for forming the QW structure and migrate up to the NR top, may return to the gap region. The rest of the atoms escapes from the gap regions and is carried away by the flow gas. Such an atom migration scenarios are depicted schematically in Fig. 13(a). In this figure, the atom supply from above is depicted by the curved thin arrows with the supply rate (per unit area) being denoted by  $\gamma$ . The atom migration routes in the gap volume are depicted by the thicker arrows. The total atom escape rate from the gap volume is defined as  $\eta$ . It is noted that the gap volume is defined as the planar area surrounded by the neighboring three NRs, i.e., the green areas shown in Figs. 13(b) and 13(c) for the side-by-side and edge-to-edge patterns, respectively, multiplied by the NR height  $h$ . The planar area surrounded by the three neighboring NRs for either side-by-side or edge-to-edge

pattern is  $3^{1/2}(d^2 - a^2)/4$ . Therefore, the atom supply rate for the total gap volume is  $3^{1/2}(d^2 - a^2)/4$ . Because the total sidewall area surrounding this gap volume in either side-by-side or edge-to-edge pattern is  $3^{1/2}ah$ , the atom supply rate per unit sidewall area is  $[3^{1/2}(d^2 - a^2)/4 - \eta]/(3^{1/2}ah)$ . If we can assume negligible atom escape from the gap volume, i.e.,  $\eta = 0$ , the atom supply rate per unit sidewall area is  $(d^2 - a^2)/(4ah)$ . It is noted that the thickness of the QW structure is expected to be proportional to the atom supply rate per unit sidewall area if  $\eta$  is assumed to be zero. Hence, based on this model, if atom escape can be neglected, the thickness ratio of the sidewall QW structure of sample I over that of sample IV is  $\sim 0.5$  at the beginning of QW growth. This value keeps increasing during the growth of the QW structure to reach  $\sim 0.57$  at the end of this growth process. Such a ratio is smaller than the experimental result of 0.68 (27.5/40.5) after the QW growth process is completed. The difference can be attributed to the non-zero atom escape rate. Also, the  $\eta$  value in sample I can be smaller than that of sample IV because the gap volume in sample I is deeper than that of sample IV. By assuming that  $\eta = 0$ , based on the model, the thickness ratio of the QW structure of sample I over that of sample II is  $\sim 1.4$  at the beginning of QW growth. This value is significantly larger than the experimental result of unity (see Table I) due to the larger  $\eta$  value in sample I, when compared with sample II, because of the wider gap between two neighboring NRs in sample I. Therefore, although the thickness variation of the sidewall QW structure is dominated by the factor of NR height, as indicated by the data in Table I, the dynamics of supplied atom migration in the gap volume can be quite complicated and plays a crucial role.

The CL emission wavelengths shown in Table II are controlled by two important factors, including the indium incorporation efficiency (the indium composition of the QW) and the QW thickness. A higher indium composition leads to a longer emission wavelength while a thinner well layer results in a shorter emission wavelength due to the effect of quantum confinement. In each of the six samples, the emission wavelength of the sidewall QWs (see the row for PV-r in Table II) is about the same as that of the top-face QWs (see the row for PV-c in Table II). The indium compositions and well layer thicknesses of the sidewall and top-face QWs in a similar sample have been analyzed with the strain state analysis technique based on atomic TEM observation.<sup>8</sup> It was found that the indium composition of the top-face QWs is significantly lower and their well layer thickness is significantly larger, when compared with the sidewall QWs. The combination of the two factors leads to the similar emission wavelengths between the top-face and sidewall QWs. It was also found that the indium composition (well layer thickness) of the sidewall QWs increases (decreases) with height on the sidewall. In this situation, the factor of indium composition dominates for emitting the longer wavelength near the top of the sidewall. This trend is consistent between samples I and IV (see the rows of CS-t, CS-m, and CS-b in Table II). It is interesting to see that the variation range of the emission wavelength along the sidewall height is larger in sample I, indicating that the sidewall QW structure varies more dramatically on a higher NR.

Suppose that the well layer thickness is proportional to the thickness of the whole QW structure. The longest sidewall emission wavelength of sample IV, when compared with other samples, can be due to its high indium composition and weak

quantum confinement. As discussed earlier, the high indium composition and large well layer thickness on the sidewall are due to the smaller sidewall area or NR height in sample IV. The shorter emission wavelengths of the top-face QWs in samples II, III, V, and VI, when compared with samples I and IV, are attributed to the smaller NR cross-sectional sizes such that the collected indium contents from the supplied atoms are relatively smaller. The shorter emission wavelengths of the sidewall QWs in samples II, III, V, and VI, when compared with sample I, are due to their smaller gap volumes such that the amounts of supplied indium atoms are relatively smaller. In samples II, III, V, and VI, the thicknesses of the sidewall QW structures are about the same as that of sample I, implying that their Ga and N supplies for growing the sidewall QWs are approximately the same. However, the chemical source for supplying indium atoms may have a different dynamics behavior in the gap volume, leading to smaller indium contents in samples II, III, V, and VI. Nevertheless, this issue deserves further investigation.

From Table I, one can see that the samples (samples V and VI) with the edge-to-edge pattern have slightly smaller cross-sectional sizes of GaN NRs and QW NRs, when compared with those of the individual samples with the side-by-side pattern of the same patterned hole diameter and pitch. Also, from Table II, the CL emission wavelengths of the samples with the edge-to-edge pattern are shorter than the corresponding samples with the side-by-side pattern. It is difficult to give a good explanation for such variations in NR cross-sectional size and CL emission wavelength. Further investigation is required.

## 6. Conclusions

In summary, we have compared the cross-sectional sizes of the GaN NR and InGaN/GaN QW NR samples of different heights and different pattern orientations, which were grown on the patterned templates of different hole diameters, pitches, and crystal orientations. The cross-sectional size of the GaN NR was mainly controlled by the patterned hole diameter and relied weakly on the NR height, pitch, and pattern orientation. The thickness of the sidewall QW structure was mainly affected by the NR height and was weakly influenced by the patterned hole diameter, pitch, and pattern orientation. The cross-sectional size variation of GaN NR was interpreted by the quasi-three-dimensional nature of atom supply amount for precipitating a 2-D disk-shaped NR segment. The variation of the sidewall QW structure was explained by the condition of constituent atom supply in the gap volume between the neighboring NRs. Also, we have compared the plan-view and cross-sectional CL emission wavelengths, including the large-scale and local measurements, among those samples. The emission wavelength depended on the NR height, cross-sectional size, pitch of the pattern, and pattern orientation. Generally speaking, the QW NRs with a smaller height, a larger cross-sectional size, or a larger pitch had a longer emission wavelength.

## References:

1. Y. S. Chen, W. Y. Shiao, T. Y. Tang, W. M. Chang, C. H. Liao, C. H. Lin, K. C. Shen, C. C. Yang, M. C. Hsu, J. H. Yeh, and T. C. Hsu, *J. Appl. Phys.* **106**, 023521 (2009).
2. R. Colby, Z. Liang, I. H. Wildeson, D. A. Ewoldt, T. D. Sands, R. E. García, and E.

- A. Stach, *Nano Lett.* **10**, 1568 (2010).
3. A. Waag, X. Wang, S. Fündling, J. Ledig, M. Erenburg, R. Neumann, M. A. Suleiman, S. Merzsch, J. Wei, S. Li, H. H. Wehmann, W. Bergbauer, M. Straßburg, A. Trampert, U. Jahn, and H. Riechert, *Phys. Status Solidi C* **8**, 2296 (2011).
  4. S. Li and A. Waag, *J. Appl. Phys.* **111**, 071101 (2012).
  5. H. Sekiguchi, K. Kishino, and A. Kikuchi, *Appl. Phys. Lett.* **96**, 231104 (2010).
  6. W. Bergbauer, M. Strassburg, Ch. Kölper, N. Linder, C. Roder, J. Lähnemann, A. Trampert, S. Fündling, S. F. Li, H. H. Wehmann, and A. Waag, *Nanotechnology* **21**, 305201 (2010).
  7. R. Koester, J. S. Hwang, D. Salomon, X. Chen, C. Bougerol, J. P. Barnes, D. S. Dang, L. Rigutti, A. de Luna Bugallo, G. Jacopin, M. Tchernycheva, C. Durand, and J. Eymery, *Nano Lett.* **11**, 4839 (2011).
  8. C. H. Liao, W. M. Chang, H. S. Chen, C. Y. Chen, Y. F. Yao, H. T. Chen, C. Y. Su, S. Y. Ting, Y. W. Kiang, and C. C. Yang, *Opt. Express* **20**, 15859 (2012).
  9. T. Yeh, Y. Lin, L. S. Stewart, P. D. Dapkus, R. Sarkissian, J. D. O'Brien, B. Ahn, and S. R. Nutt, *Nano Lett.* **12**, 3257 (2012).
  10. J. R. Chang, S. P. Chang, Y. J. Li, Y. J. Cheng, K. P. Sou, J. K. Huang, H. C. Kuo, and C. Y. Chang, *Appl. Phys. Lett.* **100**, 261103 (2012).
  11. F. Qian, Y. Li, S. Gradecak, D. Wang, C. J. Barrelet, and C. M. Lieber, *Nano Lett.* **4**, 1975 (2004).
  12. S. K. Lim, M. Brewster, F. Qian, Y. Li, C. M. Lieber, and S. Gradecak, *Nano Lett.* **9**, 3940 (2009).
  13. H. S. Chen, D. M. Yeh, Y. C. Lu, C. Y. Chen, C. F. Huang, T. Y. Tang, C. C. Yang, C. S. Wu, and C. D. Chen, *Nanotechnology* **17**, 1454 (2006).
  14. C. Y. Wang, L. Y. Chen, C. P. Chen, Y. W. Cheng, M. Y. Ke, M. Y. Hsieh, H. M. Wu, L. H. Peng, and J. J. Huang, *Opt. Express* **16**, 10549 (2008).
  15. Q. Li and G. T. Wang, *Appl. Phys. Lett.* **97**, 181107 (2010).
  16. S. Albert, A. Bengoechea-Encabo, P. Lefebvre, M. A. Sanchez-Garcia, E. Calleja, U. Jahn, and A. Trampert, *Appl. Phys. Lett.* **99**, 131108 (2011).
  17. M. Y. Ke, C. Y. Wang, L. Y. Chen, H. H. Chen, H. L. Chiang, Y. W. Cheng, M. Y. Hsieh, C. P. Chen, and J. J. Huang, *IEEE J. Sel. Top. Quantum Electron.* **15**, 1242 (2009).
  18. T. Y. Tang, W. Y. Shiao, C. H. Lin, K. C. Shen, J. J. Huang, S. Y. Ting, T. C. Liu, C. C. Yang, C. L. Yao, J. H. Yeh, T. C. Hsu, W. C. Chen, H. C. Hsu, and L. C. Chen, *J. Appl. Phys.* **105**, 023501 (2009).
  19. T. Y. Tang, C. H. Lin, Y. S. Chen, W. Y. Shiao, W. M. Chang, C. H. Liao, K. C. Shen, C. C. Yang, M. C. Hsu, J. H. Yeh, and T. C. Hsu, *IEEE Trans. Electron. Dev.* **57**, 71 (2010).
  20. A. D. L. Bugallo, L. Rigutti, G. Jacopin, F. H. Julien, C. Durand, X. J. Chen, D. Salomon, J. Eymery, and M. Tchernycheva, *Appl. Phys. Lett.* **98**, 233107 (2011).
  21. G. Jacopin, A. D. L. Bugallo, P. Lavenus, L. Rigutti, F. H. Jullien, L. F. Zagonel, M. Kociak, C. Durand, D. Salomon, X. J. Chen, J. Eymery, and M. Tchernycheva, *Appl. Phys. Express* **5**, 014101 (2012).
  22. W. Guo, M. Zhang, A. Banerjee, and P. Bhattacharya, *Nano Lett.* **10**, 3355 (2010).
  23. W. Guo, A. Banerjee, P. Bhattacharya, and B. S. Ooi, *Appl. Phys. Lett.* **98**, 193102 (2011).

24. H. Lin, Y. Lu, H. Chen, H. Lee, and S. Gwo, Appl. Phys. Lett. **97**, 073101 (2010).
25. Y. J. Hong, C. H. Lee, A. Yoon, M. Kim, H. K. Seong, H. J. Chung, C. Sone, Y. J. Park, and G. C. Yi, Adv. Mater. **23**, 3284 (2011).
26. S. Li, X. Wang, S. Fündling, M. Erenburg, J. Ledig, J. Wei, H. H. Wehmann, A. Waag, W. Bergbauer, M. Mandl, M. Strassburg, A. Trampert, U. Jahn, H. Riechert, H. Jönen, and A. Hangleiter, Appl. Phys. Lett. **101**, 032103 (2012).
27. R. Koester, J. S. Hwang, C. Durand, D. Le Si Dang and J. Eymery, Nanotechnology **21**, 015602 (2010).
28. X. J. Chen, G. Perillat-Merceroz, D. Sam-Giao, C. Durand, and J. Eymery, Appl. Phys. Lett. **97**, 151909 (2010).
29. W. Bergbauer, M. Strassburg, C. Kolper, N. Linder, C. Roder, J. Lahmann, A. Trampert, S. Fündling, S. F. Li, H.-H. Wehmann, and A. Waag, J. Cryst. Growth **315**, 164 (2011).
30. S. F. Li, S. Fündling, X. Wang, S. Merzsch, M. A. M. Al-Suleiman, J. D. Wei, H. H. Wehmann, and A. Waag, Cryst. Growth Des. **11**, 1573 (2011).
31. X. Wang, S. Li, S. Fündling, J. Wei, M. Erenburg, H. Wehmann, and A. Waag, Cryst. Growth Des. **12**, 2552 (2012).
32. K. Choi, M. Arita, and Y. Arakawa, J. Cryst. Growth **357**, 58 (2012).
33. S. D. Hersee, X. Sun, and X. Wang, Nano Lett. **6**, 1808 (2006).
34. R. K. Debnath, R. Meijers, T. Richter, T. Stoica, R. Calarco, and H. Luth, Appl. Phys. Lett. **90**, 123117 (2007).
35. J. Ristić, E. Calleja, S. Fernandez-Garrido, L. Cerutti, A. Trampert, U. Jahn, and K. H. Ploog, J. Cryst. Growth **310**, 4035 (2008).

Table I Sample parameters and the cross-sectional sizes of various samples.

Sample	I	II	III	IV	V	VI
Hole pattern (nm/nm)	250/700	180/500	180/400	250/700	180/500	180/400
Hexagon orientation	SS	SS	SS	SS	EE	EE
GaN NR height (nm)/ (growth cycle number)	~1000 (37)	~1000 (37)	~1000 (37)	~500 (18)	~1000 (37)	~1000 (37)
GaN NR cross-sectional size (nm)	376	242	243	376	239	243
Cross-sectional size increment (nm)	126	62	63	126	59	63
QW NR cross-sectional size (nm)	431	297	294	457	285	289
Sidewall QW structure thickness (nm)	27.5	27.5	25.5	40.5	23	23

Table II CL spectral peak wavelengths of various cases in different samples.

Sample	I	II	III	IV	V	VI
PV (nm)	444	432	426	452	424	418
PV-c (nm)	442	434	424	454	426	416
PV-r (nm)	444	432	426	452	424	418
CS (nm)	436	--	--	450	--	--
CS-t (nm)	444	--	--	454	--	--
CS-m (nm)	434	--	--	448	--	--
CS-b (nm)	422	--	--	444	--	--

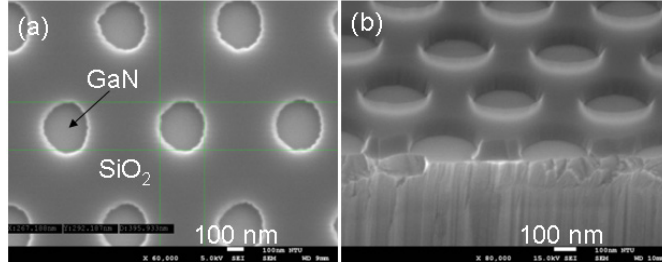


Fig. 1 Plan-view (a) and 30°-tilted (b) SEM images, respectively, of the 250/700 hole pattern.

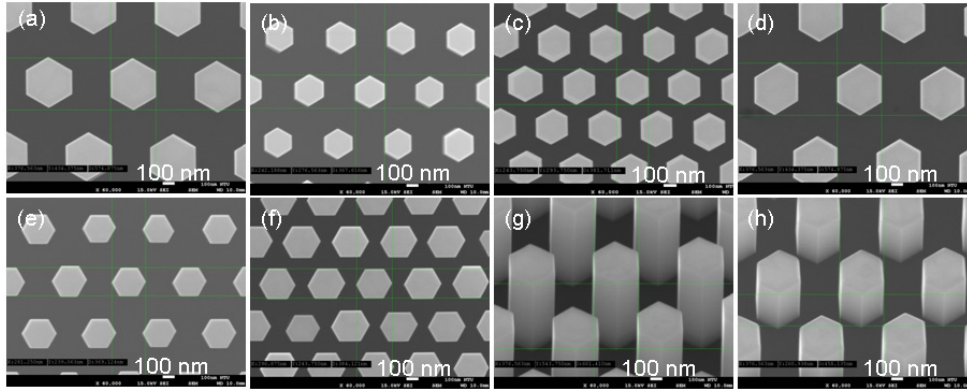


Fig. 2 (a)-(f): Plan-view SEM images of samples I-VI, respectively. (g) and (h): 30°-tilted SEM images of samples I and IV, respectively.

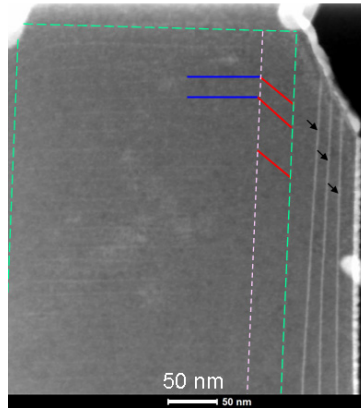


Fig. 3 Cross-sectional HAADF image of a QW NR of sample I. The three QWs near the sidewall on the right-hand side are indicated by short arrows. The greenish long-dashed lines indicate the boundary of the GaN NR. A quasi-periodic bright line pattern in the image portion of the GaN NR can be seen to show the pulsed growth process. The two horizontal continuous (blue) lines are drawn along the line pattern to indicate the thickness of a pulsed-growth period (~27 nm). Between the vertical (greenish) long-dashed line on the right and the vertical (pink) short-dashed line, the image line pattern becomes tilted, as indicated by the three slant continuous (red) lines.



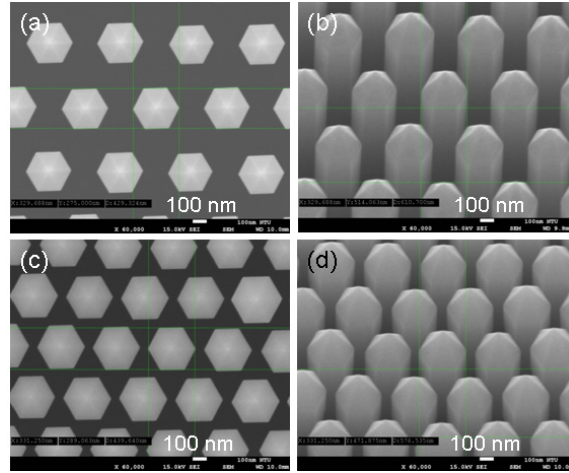


Fig. 4 (a) and (b): Plan-view SEM images with two different scales of the QW NR structure of sample I. (c) and (d): 30°-tilted SEM images with two different scales of the QW NR structure of sample I. (e) and (f): Plan-view SEM images of the QW NRs of samples II and III, respectively. (g) and (h): Plan-view and 30°-tilted SEM images, respectively, of the QW NRs of sample IV.

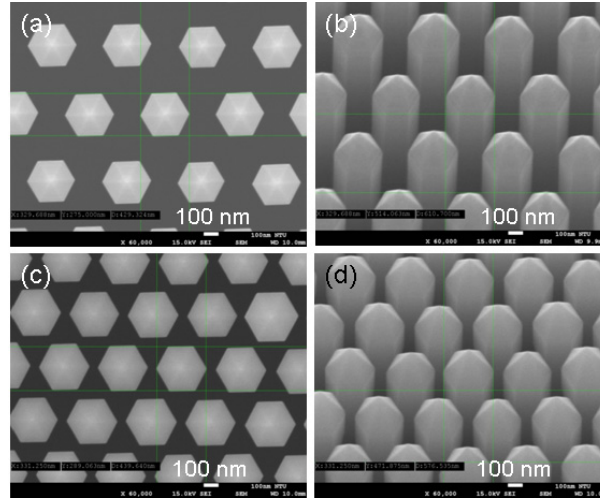


Fig. 5 (a) and (b): Plan-view and 30°-tilted SEM images of the QW NRs of sample V, respectively. (c) and (d): Plan-view and 30°-tilted SEM images of the QW NRs of sample VI, respectively.

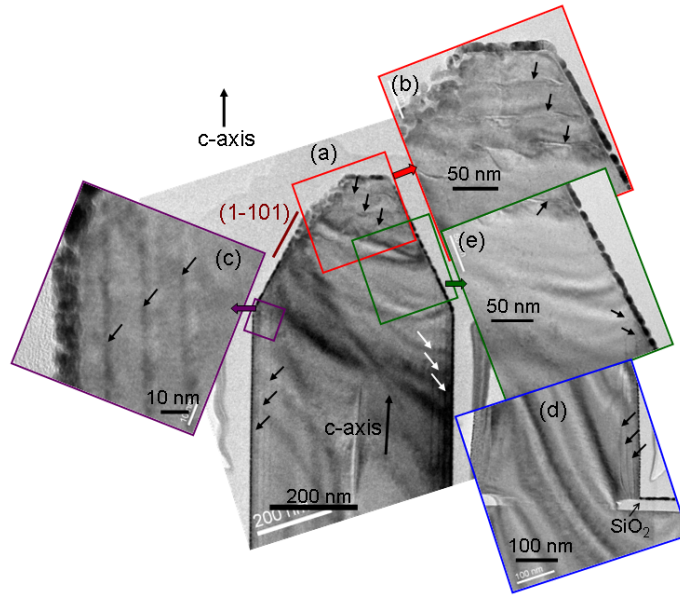


Fig. 6 (a): TEM image of a QW NR. (b)-(d): Magnified TEM images around the top, the sidewall near the top, and the sidewall near the bottom (not shown in part (a)), respectively. (e): TEM image of the slant facet (the (1-101) plane). The QWs are indicated by arrows.

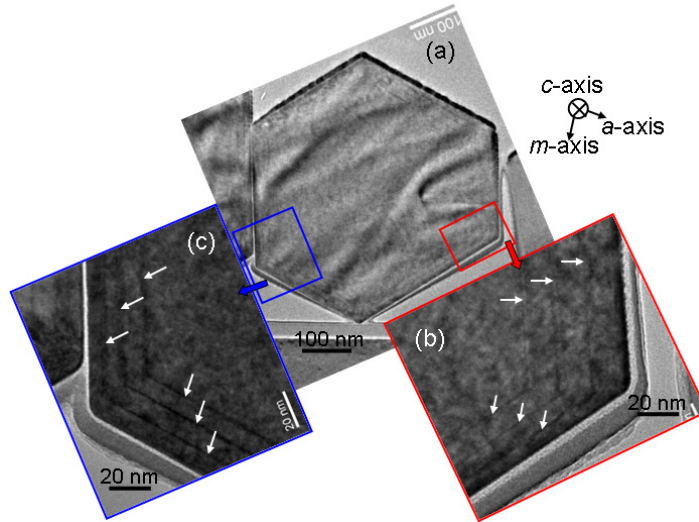


Fig. 7 (a)-(c): Cross-sectional TEM images of a QW NR, which fell during TEM specimen preparation.

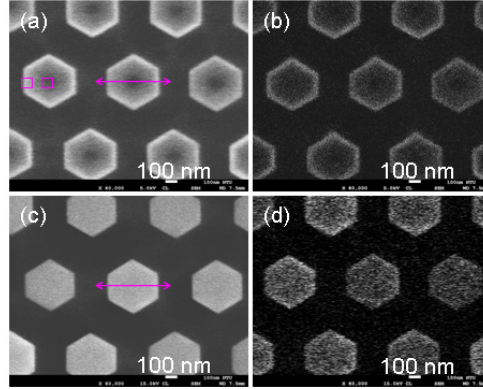


Fig. 8 (a) and (b): Plan-view CL mapping images with the panchromatic spectrum and the emission wavelength at 444 nm, respectively, of sample I when the electron acceleration voltage is 5 kV. (c) and (d): Similar CL images to parts (a) and (b), respectively, except that the electron acceleration voltage is 15 kV.

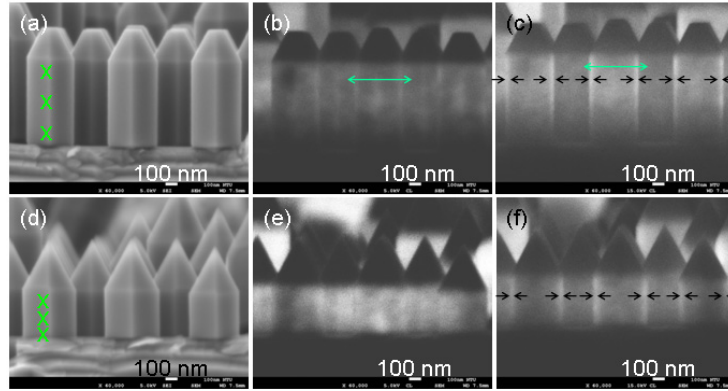


Fig. 9 (a)-(c): Cross-sectional SEM image at 5 kV in electron acceleration voltage, and co-located panchromatic CL mapping images at 5 and 15 kV in electron acceleration voltages, respectively, of sample I. (d)-(f): Cross-sectional SEM image at 5 kV in electron acceleration voltage, and co-located panchromatic CL mapping images at 5 and 15 kV in electron acceleration voltages, respectively, of sample IV.

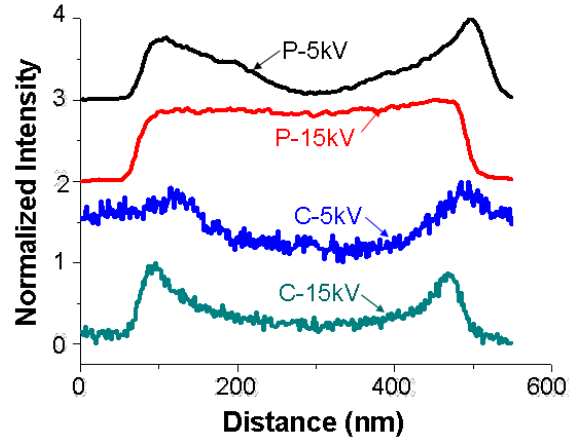


Fig. 10 Line-scan intensity profiles (from top to bottom) along the double-headed arrows in Figs. 8(a), 8(c), 9(b), and 9(c) for sample I. The letters “P” and “C” refer to the plan-view and cross-sectional observations, respectively.

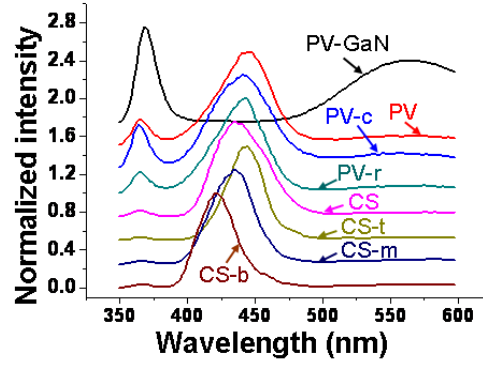


Fig. 11 CL spectra of sample I measured at different locations and different view directions, including that from the large-scale plan-view (PV) measurement, that at the center on the top face of an NR (PV-c), that at the rim on the top face of the NR (PV-r), that from the large-scale cross-sectional (CS) measurement, that at a point near the top of the sidewall of an NR (CS-t), near the middle height of the sidewall of the NR (CS-m), and near the bottom of the sidewall of the NR (CS-b).

For comparison, the plan-view CL spectrum of the bare GaN NR array is also plotted as curve PV-GaN.

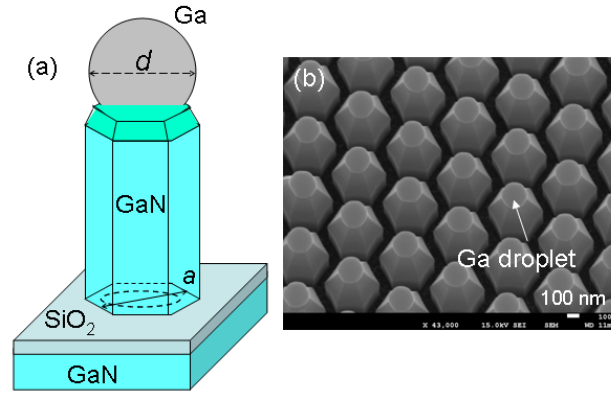


Fig. 12 (a): Schematic drawing for a model of the self-catalytic VLS growth. (b): 30°-tilted SEM image taken from a sample when the growth stops at the end of the first half-cycle of Ga source supply in pulsed growth.

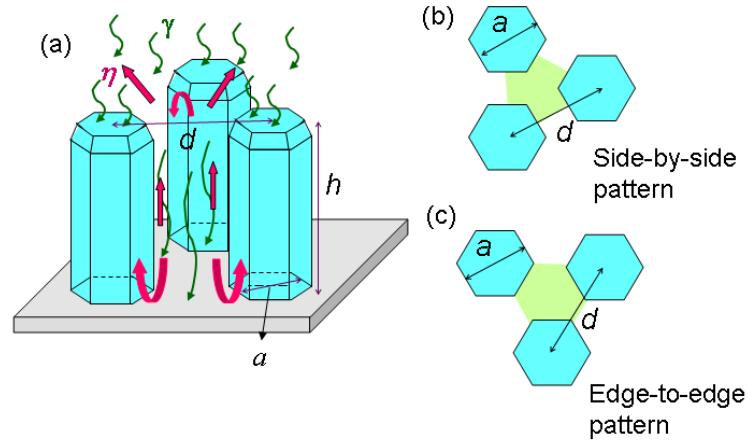


Fig. 13 (a): Schematic drawing of atom migration scenarios. The atom supply from the top is depicted by the curved thin arrows with the supply rate (per unit area) being denoted by  $\gamma$ . The atom migration routes in the gap volume are depicted by the thicker arrows. The total atom escape rate from the gap volume is defined as  $\eta$ . The gap volume is defined as the planar area surrounded by the neighboring three NRs, i.e., the green areas shown in parts (b) and (c) for the side-by-side and edge-to-edge patterns, respectively, multiplied by the NR height  $h$ .

## **Part II: Regularly Patterned ZnO Nanorods Grown with the Hydrothermal Method**

### **1. Introduction**

Because of its large band gap of 3.36 eV and high exciton binding energy of 60 meV, ZnO nanostructures have attracted much research attention for nano-device applications, including light-emitting devices,<sup>1</sup> solar cells,<sup>2</sup> power generators,<sup>3</sup> and others.<sup>4</sup> ZnO nanostructures, such as nanorods (NRs),<sup>5</sup> nanowires,<sup>6</sup> nanotubes,<sup>7</sup> and nanowalls,<sup>7</sup> have been widely investigated over the past few years due to their superior electrical and optical properties. In the device applications of ZnO NRs, it is important not only to synthesize the ZnO NRs with a high degree of regularity and uniformity in terms of their height and cross-sectional size, but also to accurately control their positions. The controls of NR position and shape can enhance the performances of the fabricated electronics and optoelectronics devices.<sup>8,9</sup> A few vapor-phase methods have been used for the growth of ZnO NRs, including metalorganic chemical vapor deposition (MOCVD),<sup>10</sup> pulsed laser deposition,<sup>11</sup> and radio-frequency magnetron sputtering.<sup>12</sup> ZnO NR formed via the hydrothermal method has attracted much attention due to its advantages of low-temperature growth (<100 °C), and rapid, large-scale, and low-cost operation. Selective-area growth (SAG) on a patterned mask has been proved to be an effective method for localizing the growth of ZnO nanostructures. Various lithography methods for SAG patterning have been reported, including nano-imprint,<sup>13</sup> interference,<sup>14</sup> electron-beam writing,<sup>15</sup> and nanosphere coating.<sup>16</sup> For a high-throughput, low-cost, and large-area fabrication, nano-imprint lithography is a preferred choice.

Although the growth of ZnO NRs with the hydrothermal method has the aforementioned advantages, it may lead to a high defect density due to its low growth temperature. In particular, recently it has been reported that void structures could be formed in ZnO grown with the hydrothermal method.<sup>17-19</sup> However, although the existences of voids in the ZnO films,<sup>17</sup> on ZnO NR surface,<sup>18</sup> and inside ZnO NRs after thermal annealing were mentioned,<sup>19</sup> so far no detailed study on the void distributions inside ZnO NRs and their formation conditions and mechanisms was reported, particularly in regularly patterned ZnO NRs grown with the hydrothermal method. In this paper, we first demonstrate the growth of regularly patterned ZnO NR arrays on GaN template with the hydrothermal method based on the nano-imprint lithography technique. The optimum conditions of the concentration of growth solution, growth temperature, and growth duration are achieved. Then, with scanning electron microscopy (SEM), backscattering electron microscopy (BSEM), and transmission electron microscopy (TEM), including the observations of high-angle annular dark-field (HAADF) and energy dispersive X-ray spectrum (EDX), the void distributions and their formation mechanisms under various thermal annealing and doping conditions are investigated. Also, the emission properties under various conditions are explored with photoluminescence (PL) measurement.

In section 2 of this paper, the fabrication procedures and growth conditions of regularly patterned ZnO NR arrays are reported. The void structures under different thermal annealing and doping conditions are discussed in section 3. Then, the optical characterization results are shown in section 4. Discussions regarding the formation

of voids are given in section 5. Finally, conclusions are drawn in section 6.

## 2. Growth of Regularly Patterned ZnO Nanorod Arrays

The ZnO NR arrays are grown on a patterned  $\text{Si}_3\text{N}_4$  mask layer of 40 nm in thickness, which is deposited with plasma enhanced chemical vapor deposition on an un-doped GaN layer of 2  $\mu\text{m}$ . The GaN layer is grown with MOCVD at 1000  $^\circ\text{C}$  on a *c*-plane sapphire substrate. The nano-imprint lithography technique is used for patterning the  $\text{Si}_3\text{N}_4$  mask with a triangular arrangement of holes of 350 nm in hole diameter and 1453 nm in pitch. Figure 1(a) shows the plan-view SEM image (with a JEOL JSM-7001F system at 15 kV in electron acceleration voltage) of the patterned template used for ZnO NR growth. In the hydrothermal growth process, after cleaning such a template is placed upside down in the growth solution for avoiding the accumulation of precipitates in the gaps between NRs. For un-doped ZnO NR growth, the aqueous solution for the hydrothermal reaction consists of equal-molar zinc nitrate hexahydrate and hexamethylenetetramine of controlled concentrations. Before use, the chemicals are well mixed in the solution and the precipitates are filtered. The template is immersed in the solution 10 min after the solution is heated to the designated growth temperature. Then, the sealed beaker containing the growth solution and the template is kept at the designated growth temperature for the designated growth duration.

Figures 1(b)-1(d) show the 30 $^\circ$ -tilted SEM images of the growth results on the template with the growth durations of 10, 30, and 180 min, respectively, when the concentration of the growth solution is 0.08 M and the growth temperature is 80  $^\circ\text{C}$ . As shown in Fig. 1(b), multiple ZnO nucleation clusters are formed in each hole of the patterned mask after the growth duration of 10 min. Each of those nucleation clusters can extend its length along the *c*-axis to form a small NR, as shown in Fig. 1(c). As the growth duration becomes longer, those small ZnO NRs in a hole can merge into a large hexagonal NR with the cross-sectional size larger than the hole diameter, as shown in Fig. 1(d). The larger cross-sectional size of the grown NRs implies that both the vertical growth (along the *c*-axis) and lateral growth (along the *m*-axis) of ZnO occur during the formation of an NR. Here, one can see that the top faces of the NRs are quite flat. The cross-sectional size (the distance between two parallel sides of the hexagonal shape) is about 850 nm. The height of this ZnO NR array is around 2  $\mu\text{m}$ . Figure 1(e) shows a larger-scale tilted SEM image of the same sample illustrating the uniformity of the ZnO NR array. It is found that the ZnO NR growths with higher growth solution concentrations (say, 0.1 M), higher growth temperatures (say, 95  $^\circ\text{C}$ ), or longer growth durations (say, 300 min) lead to coalesced growth of NRs to form thin films. In the hydrothermal reaction study, we also consider the growth of n-ZnO NR arrays by doping ZnO with Ga through the addition of gallium nitrate hydrate to the growth solution of various concentrations. Figure 1(f) shows the tilted SEM image of a Ga-doped ZnO NR array sample under the same growth conditions as those for Figs. 1(b)-1(e). The Ga doping is implemented by adding gallium nitrate hydrate of a designated concentration into the growth solution. The used concentration of gallium nitrate hydrate for growing the sample shown in Fig. 1(f) is 0.003 M. The cross-sectional size of the Ga-doped ZnO NRs is smaller than that of the un-doped NRs. The electron concentration of the grown n-ZnO (a thin film growth of 300 min in growth duration) under the same

growth conditions as those for the sample in Fig. 1(f) is measured to give  $2.57 \times 10^{19} \text{ cm}^{-3}$ .

As shown in Fig. 1(c), an NR is formed through the growth of multiple small rod structures first and then their mergence. Figures 2(a) and 2(b) show a cross-sectional TEM image of an NR and the close-up image around the bottom of the NR, respectively. The TEM sample is prepared through the sample ablation by a focused ion beam. The TEM investigation is performed using a Philips Tecnai F30 field-emission electron microscope with an accelerating voltage of 300 kV and a probe forming lens of  $C_s = 1.2 \text{ mm}$ . In Fig. 2(b), the dark line pattern dividing different domains indicates the merging process of the multiple nucleation clusters. During this process, the domain boundaries may involve into threading dislocations when the domains are merged and the growth is continued. In Fig. 2(b), two dislocations are formed as indicated by the white arrows. As shown in Fig. 2(a), one of them propagates to the top of the NR. The other moves toward the upper-left direction. In this image, this dislocation stops at the boundary between two regions of different levels of surface roughness. As roughly divided by the two dashed curves in Fig. 2(a), the relatively smoother and rougher regions correspond to the portions of vertical (along the *c*-axis) and lateral (along the *m*-axis) growths, as to be further discussed later. The left dislocation in Fig. 2(a) can be bended in the lateral growth region such that it does not propagate toward the NR top.

### 3. Void Formation in Nanorods

Thermal annealing can improve the crystal and optical qualities of the grown ZnO NRs. Figures 3(b)-3(e) show the cross-sectional TEM images of un-doped ZnO NRs after thermal annealing with ambient oxygen for 60 min at 200, 300, 400, and 500 °C, respectively. The un-doped ZnO NRs are grown with 0.08 M in solution concentration at 80 °C for 180 min. For comparison, the TEM image of an as-grown sample is also shown in Fig. 3(a). In the as-grown sample, no void structure can be seen in the ZnO NR. However, voids are formed after thermal annealing. At 200 °C in annealing temperature, the voids are small such that the image contrast is weak. A few voids are indicated by the arrows. Here, the voids are distributed around the lower central portion of the NR. As the annealing temperature increases, the void size and density become larger and its distribution extends upward. However, with the annealing temperatures at 300 and 400 °C, the voids are distributed only in the region of vertical growth. In Figs. 3(c) and 3(d), the dashed curves again indicate roughly the boundaries between the regions of vertical and lateral growths. When the annealing temperature is 500 °C, the void distribution reaches the top of the NR and extends into the region of lateral growth. As shown in Figs. 3(d) and 3(e), the void size can be as large as 100 nm.

The scenarios of void formation in Ga-doped ZnO NRs are quite different. Figures 4(a)-4(d) show the cross-sectional TEM images of an as-grown doped ZnO NR, and doped ZnO NRs thermally annealed at 200, 300, and 400 °C, respectively, with ambient oxygen for 60 min. The doped ZnO NRs are grown with 0.08 M in solution concentration and 0.003 M in doping concentration (the concentration of gallium nitrate hydrate) at 80 °C for 180 min. Here, one can see that no void exists in the as-grown sample. Also, void is essentially not formed with the annealing temperature at 200 °C. Voids are clearly seen when the annealing temperature



becomes higher, as shown in Figs. 4(c) and 4(d). Therefore, voids can be formed in a Ga-doped ZnO NR when it is annealed at a higher temperature, when compared with an un-doped ZnO NR.

The void structures in the NRs can also be seen with the observation of BSEM. Figure 5(a) shows the SEM image of four fallen un-doped ZnO NRs before thermal annealing. The SEM image of the same sample after thermal annealing at 300 °C for 60 min with ambient oxygen is shown in Fig. 5(b). The SEM image of the same sample after the second annealing process at 400 °C for 60 min with ambient oxygen is shown in Fig. 5(c). Then, The SEM image of the same sample after the third annealing process at 500 °C for 60 min with ambient oxygen is shown in Fig. 5(d). Here, one can see that void cannot be observed with SEM either before or after thermal annealing. However, voids can be observed with BSEM, as shown in Figs. 5(f)-5(h). Figures 5(e)-5(h) show the BSEM images corresponding to the SEM images in Figs. 5(a)-5(d), respectively. The dark spots in Figs. 5(f)-5(h) show the void distributions under different annealing conditions. The SEM images in Figs. 6(a) and 6(b) show either the bottom or top faces of a few un-doped ZnO NRs after the three-stage annealing process (300, 400, and then 500 °C). In a bottom face, one can see a circular protrusion, which corresponds to the ZnO portion in the patterned hole on the growth template. Figures 6(c) and 6(d) show the corresponding BSEM images of Figs. 6(a) and 6(b), respectively. Here, one can see that on the bottom faces, the voids distribute only in the protrusion portions, i.e., the portion of vertical growth. On a top face, the voids distribute in a larger circular area. This result is consistent with those in Figs. 3(e) and 4(d).

#### 4. Photoluminescence Measurement

Figure 7 shows the PL spectra of un-doped ZnO NR array samples under the as-grown condition and the thermal annealing conditions of different ambient gases (air and oxygen). The NR array samples are grown with 0.08 M in solution concentration at 80 °C for 180 min. The thermal annealing conditions include 300 °C in temperature and 60 min in duration. The PL measurement is excited by a HeCd laser at 325 nm with the incident power at 10 mW. In each curve of Fig. 7, a narrow peak around 375 nm due to the band-edge emission of ZnO and a broad hump in the range of 470-800 nm from defect emission can be observed. The small peak around 360 nm in the spectrum with ambient air originates from the band-edge emission of the GaN template. Because the spectral portions of band-edge and defect emissions can be well separated, the ratio of their individual integrated intensities can be used for representing the optical quality of the NR array sample. Here, one can see that the defect emission is significantly weaker under the annealing condition of ambient oxygen. The integrated PL intensity ratios of band-edge emission over defect emission are 0.05, 0.45, and 2.11 under the as-grown condition, the conditions of annealing with ambient air and annealing with ambient oxygen, respectively. Here, one can see that thermal annealing can improve the optical quality of a ZnO NR array sample, particularly when oxygen is used as the ambient gas. Therefore, oxygen was used as the ambient gas in the annealing processes leading to the results in Figs. 3-6.

Figure 8 shows the PL spectra of Ga-doped ZnO NR array samples under different thermal annealing conditions (different annealing temperatures). The doped

ZnO NRs are grown with 0.08 M in solution concentration and 0.003 M in doping concentration at 80 °C for 180 min. The annealing process is undertaken with ambient oxygen for 60 min. Here, one can see that the defect emission level decreases first and then increases as the annealing temperature increases from 200 to 500 °C. At 400 and 500 °C for thermal annealing, the defect emission spectral peak red shifts, indicating that the red emission defect dominates now. This result implies that the density of hydroxyl groups is reduced through thermal annealing. Therefore, the reduction of hydroxyl groups is related to the formation of voids. The contrast of intensity level between the band-edge and defect emissions is largest when the annealing temperature is 300 °C. Table 1 shows the integrated PL intensity ratios of various samples with different Ga doping concentrations when they are annealed at different temperatures. The annealing is undertaken with ambient oxygen for 60 min. Here, one can see that at the annealing temperature of 300 °C, we can always obtain the highest integrated intensity ratio under each doping condition. The ratio is the highest when the doping concentration is 0.003 M. Therefore, 0.003 M in gallium nitrate hydrate concentration and 300 °C in annealing temperature represent the optimum conditions for forming Ga-doped ZnO NR arrays based on the hydrothermal method as far as optical property is concerned.

## 5. Discussions

Figures 9(b)-9(d) show the HAADF images of Ga-doped ZnO NR array samples when they are thermally annealed at 200, 300, and 400 °C, respectively. For comparison, the HAADF image of the as-grown sample is also shown in Fig. 9(a). The doped ZnO NRs are grown with 0.08 M in solution concentration and 0.003 M in doping concentration at 80 °C for 180 min. The annealing process is undertaken with ambient oxygen for 60 min. In each part of Fig. 9, one can see the darker and brighter regions of vertical and lateral growths, respectively, indicating that the vertical-growth region is oxygen rich because the signal intensity in a HAADF image is proportional to average atomic number. The contrast between the vertical and lateral-growth regions diminishes as the annealing temperature becomes higher. In each of those images, a horizontal dashed line is drawn, along which EDX analysis is made. The atomic % levels of O, Zn, and Ga along the dashed lines in Figs. 9(a)-9(d) are shown in Figs. 10(a)-10(d), respectively. It is noted that in each case, the dashed line passes across the boundaries between the vertical and lateral growth regions. In each part of Fig. 10, data points 1, 2, 7, and 8 (3-6) are located in the lateral (vertical) growth region. As shown in Fig. 10(a), the oxygen atomic % is higher than that of zinc in both regions of vertical and lateral growths. The difference between the oxygen and zinc contents in the vertical-growth region is significantly larger than that in the lateral-growth region, indicating that the crystal in the lateral-growth region is closer to the stoichiometric condition. The oxygen-rich condition in the vertical-growth region is the major cause for easier formation of voids. The gallium atomic % is low and quite uniform over the two growth regions. When the sample is thermally annealed, the difference between the oxygen and zinc contents becomes smaller in either the vertical or lateral growth region. The difference becomes smaller and smaller when the annealing temperature is raised. With 400 °C in annealing temperature, both atomic % levels of oxygen and zinc become close to 50 % or the stoichiometric condition. The difference between the vertical and lateral-growth

regions diminishes due to the desorption of excess oxygen atoms during the process of thermal annealing.

As shown in Fig. 8, the defect emission level decreases at the thermal annealing temperatures of 200 and 300 °C and then increases as the annealing temperature is raised to 400 and 500 °C. It is noted that the emission spectral peak is red shifted from ~620 to ~660 nm when the annealing temperature is increased from 200 to 500 °C. The defect emission band can be split into two components, including one centered at ~590 nm (yellow emission) and the other centered at ~690 nm (red emission). The red emission in a sample grown with the hydrothermal method has known to result from oxygen interstitials.<sup>17,20</sup> The yellow emission was partly attributed to oxygen interstitials.<sup>21</sup> It was also ascribed to the presence of hydroxyl groups in the sample, which are commonly observed in a sample with a solution growth method.<sup>22</sup> The hydroxyl groups are involved in the crystallization of ZnO NRs by substituting oxygen anions at their positions.<sup>17</sup> During the annealing process, the hydroxyl groups gain the energy required to escape from their crystal lattice sites. Its desorption rate reaches the peak level at 150 °C in annealing temperature.<sup>22</sup> Hence, the reduction of hydroxyl groups in ZnO lattice may be responsible for the decrease of the yellow emission level in the PL spectra. With ambient oxygen during thermal annealing, ambient oxygen can be absorbed by the NRs while oxygen interstitials can evade from NRs at the same time. When the annealing temperature is lower than 400 °C, the process of oxygen desorption may dominate such that the red emission caused by excess oxygen becomes weak. As the annealing temperature becomes higher, the process of oxygen absorption dominates such that the red emission level becomes higher. On the other hand, during thermal annealing at high temperatures, no supply of hydroxyl groups can lead to the increase of yellow emission. It is noted that the aforementioned increase of oxygen interstitials under the conditions of 400 and 500 °C in annealing temperature can occur only in a thin surface layer on a ZnO NR, particularly near the bottom of an NR where the supply of ambient oxygen is smaller. In this situation, the increase of oxygen interstitials near the NR top can be monitored for demonstrating the increase of red emission with the PL measurement under the conditions of shallow penetration (~100 nm in depth from the NR surface) and shadowed illumination of UV excitation laser. However, in the EDX measurement with the results shown in Fig. 10, the locations of acquiring the data are close to the NR bottom (see the dashed lines in Fig. 9) where the increase of oxygen interstitials is insignificant such that the stoichiometric condition can be almost reached, as shown in Fig. 10(d).

The formation of voids can be attributed to the desorption of hydroxyl groups during the annealing process.<sup>17</sup> In the ZnO crystal with hydroxyl groups, to maintain local electrical neutrality, cation vacancies must exist to neutralize the additional positively charges of hydrogen ions in the hydroxyl groups. During thermal annealing, the hydroxyl groups leave the sample in the form of water vapor and generate anion vacancies at their originally resting sites. The cation vacancies react with the anion vacancies to form vacancy pairs. The gathering of vacancy pairs forms the cores of the voids. With the thermal energy, a few small voids can merge into a larger one at a higher annealing temperature.

The speed of vertical growth is much higher than that of lateral growth in forming ZnO NRs. The higher growth speed in the vertical direction leads to poorer

crystal quality with abundant defects.<sup>19</sup> As shown in Figs. 3 and 4, void formation can be observed in the vertical-growth region at lower thermal annealing temperatures, implying that the density of hydroxyl groups is higher in the vertical-growth region. One of the reasons for vertical growth being more defective is the polarity along the c-axis owing to the hexagonal wurtzite structure of ZnO.<sup>23</sup> The top polar plane is more attractive to hydroxyl groups when compared with the non-polar plane on the sidewall of a ZnO NR. The non-uniform void distribution along the c-axis in an NR under the condition of 300 or 400 °C in annealing temperature (see Figs. 3 and 4) can be attributed to the temperature gradient in thermally annealing the NR sample. Although the desorption rate of hydroxyl groups decreases with increasing annealing temperature beyond 150 °C,<sup>24</sup> only when the annealing temperature is high enough for the void cores to grow into small voids and for the small voids to merge into large voids such that voids can be observed with TEM. In Figs. 3(c), 3(d), and 4(c), the void cores or small voids near the NR tops are too small to be observed.

## 6. Conclusions

In summary, we have investigated the void structures and related optical properties after thermal annealing with ambient oxygen in regularly patterned ZnO NR arrays grown with the hydrothermal method. In increasing the annealing temperature, based on the TEM and BSEM observations, void distribution started from the bottom and extended to the top of an NR in the vertical (c-axis) growth region. When the annealing temperature became higher than 400 °C, void distribution spread into the lateral (m-axis) growth region. PL measurement showed that the n-ZnO band-edge emission, in contrast to defect emission in the yellow-red range, was the strongest under the n-ZnO NR process conditions of 0.08 M in growth solution concentration, 0.003 M in Ga doping concentration, 80 °C in growth temperature, 180 min in growth duration, and 300 °C in thermal annealing temperature with ambient oxygen for 60 min. EDX data indicated that the concentration of hydroxyl groups, which took the positions of anions in ZnO, in the vertical-growth region was significantly higher than that in the lateral-growth region of an NR. During thermal annealing, hydroxyl groups were desorbed from the NR leaving anion vacancies for reacting with cation vacancies to form void cores. The thermal energy provided energy for merging small voids into large ones.

## References:

1. Park, W. I.; Yi, G. C. *Adv. Mater.* **2004**, *16*, 87-90.
2. Law, M.; Greene, L. E.; Johnson, J. C.; Saykally, R.; Yang, P. D. *Nat. Mater.* **2005**, *4*, 455-459.
3. Qin, Y.; Wang, X.; Wang, Z. L. *Nature* **2008**, *451*, 809-813.
4. Huang, M. H.; Mao, S.; Feick, H.; Yan, H. Q.; Wu, Y. Y.; Kind, H.; Weber, E.; Russo, R.; Yang, P. D. *Science* **2001**, *292*, 1897-1899.
5. Lee, Y. J.; Ruby, D. S.; Peters, D. W.; McKenzie, B. B.; Hsu, J. W. P. *Nano Lett.* **2008**, *8*, 1501-1505.
6. Lee, S. W.; Jeong, M. C.; Myoung, J. M. *Appl. Phys. Lett.* **2007**, *90*, 133115.
7. Hong, Y. J.; Jung, H. S.; Yoo, J.; Kim, Y. J.; Lee, C. H.; Kim, M.; Yi, G. C. *Adv. Mater.* **2009**, *21*, 222-226.

8. Jensen, L. E.; Bjørk, M. T.; Jeppesen, S.; Persson, A. I.; Ohlsson, B. J.; Samuelson, L. *Nano Lett.* **2004**, *4*, 1961-1964.
9. Lee, C. H.; Yoo, J.; Hong, Y. J.; Cho, J.; Kim, Y. J.; Jeon, S. R.; Baek, J. H.; Yi, G. C. *Appl. Phys. Lett.* **2009**, *94*, 213101.
10. Park, W. I.; Yi, G. C.; Kim, J. W.; Park, S. M. *Appl. Phys. Lett.* **2003**, *82*, 4358-4360.
11. Sharma, A. K.; Narayan, J.; Muth, J. F.; Teng, C. W.; Jin, C.; Kvit, A. *Appl. Phys. Lett.* **1999**, *75*, 3327-3330.
12. Minemoto, T.; Negami, T.; Nishiwaki, S.; Takakura, H.; Hamakawa, Y. *Thin Solid Films* **2000**, *372*, 173-176.
13. Jung, M. H.; Lee, H. *Nanoscale Res. Lett.* **2011**, *6*, 159-169.
14. Wei, Y.; Wu, W.; Guo, R.; Yuan, D.; Das, S.; Wang, Z. L. *Nano Lett.* **2010**, *10*, 3414-3419.
15. Xu, S.; Wei, Y.; Kirkham, M.; Liu, J.; Mai, W.; Davidovic, D. *J. Am. Chem. Soc.* **2008**, *130*, 14958-14959.
16. Dong, J. J.; Zhang, X. W.; Yin, Z. G.; Zhang, S. G.; Wang, J. X.; Tan, H. R.; Gao, Y.; Si, F. T.; Gao, H. L. *ACS Appl. Mater. Interfaces* **2011**, *3*, 4388-4395.
17. Richardson, J. J.; Goh, G. K. L.; Le, H. Q.; Liew, L. L.; Lange, F. F.; DenBaars, S. P. *Cryst. Growth Des.* **2011**, *11*, 3558-3563.
18. Jeon, S. M.; Kim, M. S.; Cho, M. Y.; Choi, H. Y.; Yim, K. G.; Kim, G. S.; Kim, H. G.; Leem, J. Y. *J. Korean Phys. Soc.* **2010**, *57*, 1477-1481.
19. Stiegler, J. M.; Tena-Zaera, R.; Idigoras, O.; Chuvilin, A.; Hillenbrand, R. *Nature Comm.* **2012**, *3*, 1131-1137.
20. Cai, J. W.; Xu, J. P.; Zhang, X. S.; Niu, X. P.; Xing, T. Y.; Ji, T.; Li, L. *Optoelectron. Lett.* **2012**, *8*, 4-8.
21. Djurišić, A. B.; Leung, Y. H.; Tam, K. H.; Ding, L.; Ge, W. K.; Chen, H. Y.; Gwo, S. *Appl. Phys. Lett.* **2006**, *88*, 103107.
22. Tam, K. H.; Cheung, C. K.; Leung, Y. H.; Djurišić, A. B.; Ling, C. C.; Beling, C. D.; Fung, S.; Kwok, W. M.; Chan, W. K.; Phillips, D. L.; Ding, L.; Ge, W. K. *J. Phys. Chem. B* **2006**, *110*, 20865.
23. Kim, K. S.; Jeong, H.; Jeong, M. S.; Jung, G. Y. *Adv. Funct. Mat.* **2010**, *20*, 3055-3063.
24. Xie, R.; Sekiguchi, T.; Ishigaki, T.; Ohashi, N.; Li, D.; Yang, D.; Liu, B.; Bando, Y. *Appl. Phys. Lett.* **2006**, *88*, 134103.

**Table 1** Ratio of integrated PL intensity of the ZnO band-edge emission over that of the defect emission with different Ga doping concentrations at different thermal annealing temperatures.

Doping concentration (M)	As-grown	200 °C	300 °C	400 °C	500 °C
0.002	0.24	0.43	1.69	0.18	0.08
0.003	0.17	0.53	2.11	0.28	0.09
0.004	0.15	0.55	0.84	0.22	0.01

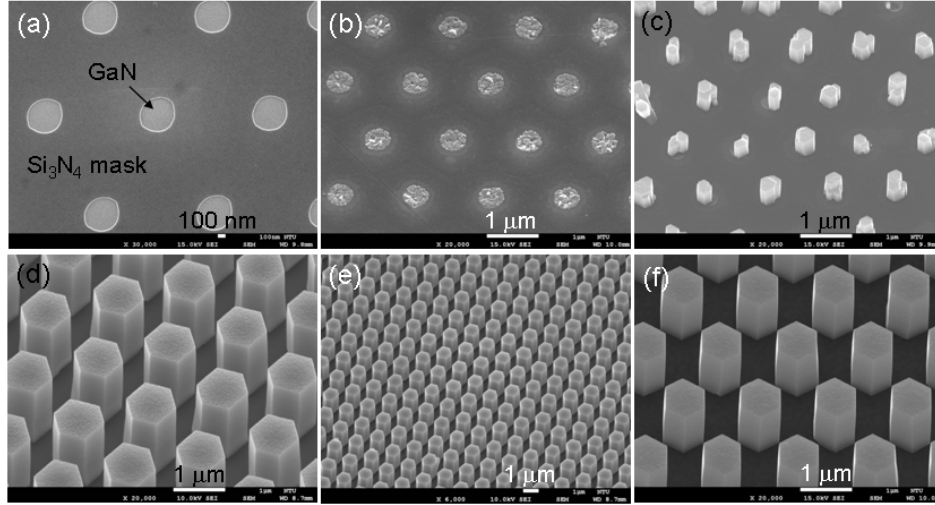


Fig. 1 (a): Plan-view SEM image of a patterned template for ZnO NR growth. (b)-(d): 30°-tilted SEM images of the growth results on the template with the growth durations of 10, 30, and 180 min, respectively, when the concentration of the growth solution is 0.08 M and the growth temperature is 80 °C. (e): Larger-scale tilted SEM image of the same sample illustrating the uniformity of the ZnO NR array. (f): Tilted SEM image of a Ga-doped ZnO NR array sample under the same growth conditions as those in parts (b)-(e).

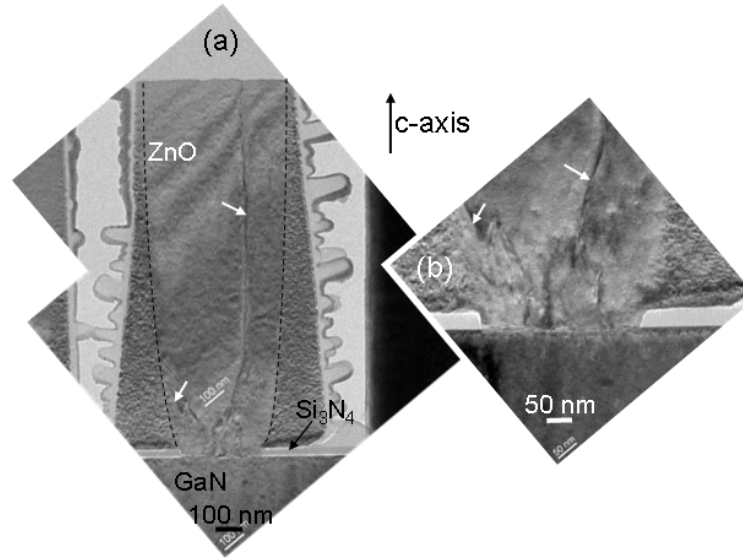


Fig. 2 (a) and (b): Cross-sectional TEM image of an NR and the close-up image around the bottom of the NR, respectively. The arrows show the two dislocations. The two dashed curves divide the regions of the vertical- and lateral-growth regions.

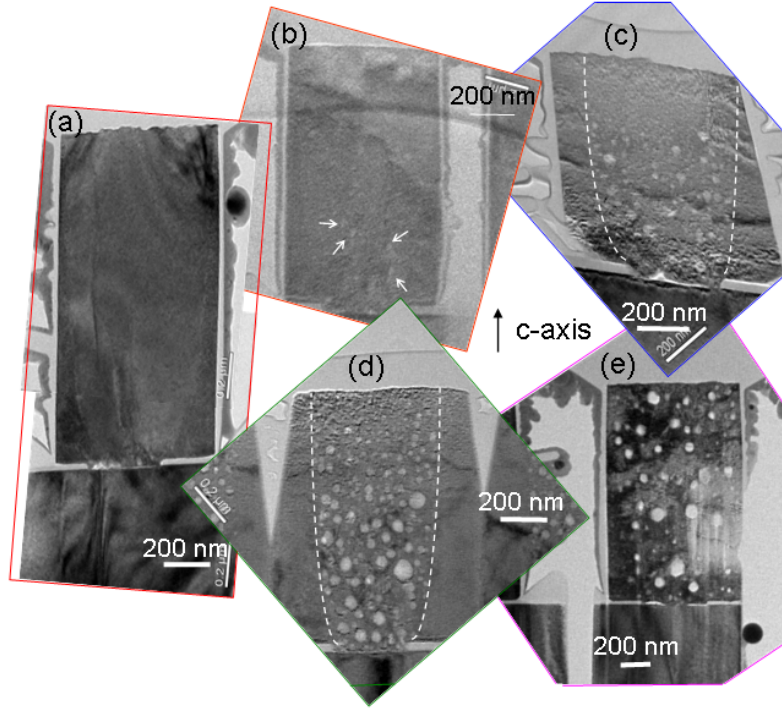


Fig. 3 (a): Cross-sectional TEM image of an as-grown un-doped ZnO NR sample. (b)-(e): Cross-sectional TEM images of un-doped ZnO NRs after thermal annealing with ambient oxygen for 60 min at 200, 300, 400, and 500 °C, respectively. The ZnO NRs are grown with 0.08 M in solution concentration at 80 °C for 180 min.

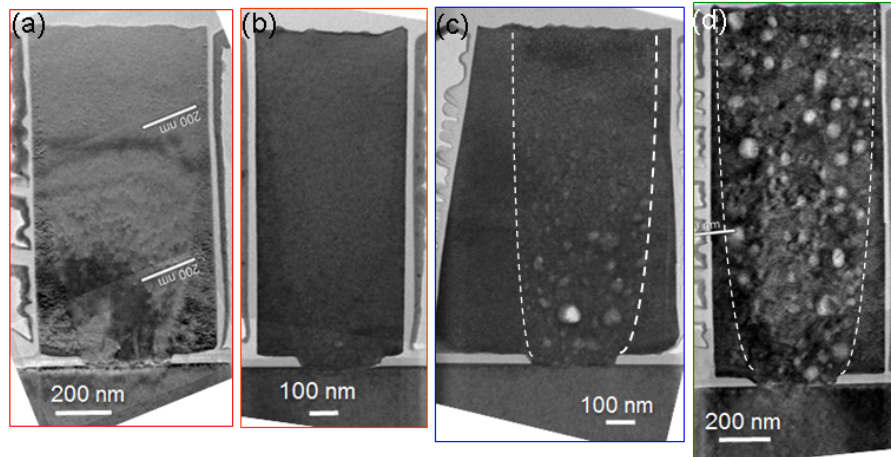


Fig. 4 (a)-(d): Cross-sectional TEM images of an as-grown Ga-doped ZnO NR, and Ga-doped ZnO NRs thermally annealed at 200, 300, and 400 °C, respectively, with ambient oxygen for 60 min. The Ga-doped ZnO NRs are grown with 0.08 M in solution concentration and 0.003 M in doping concentration at 80 °C for 180 min.

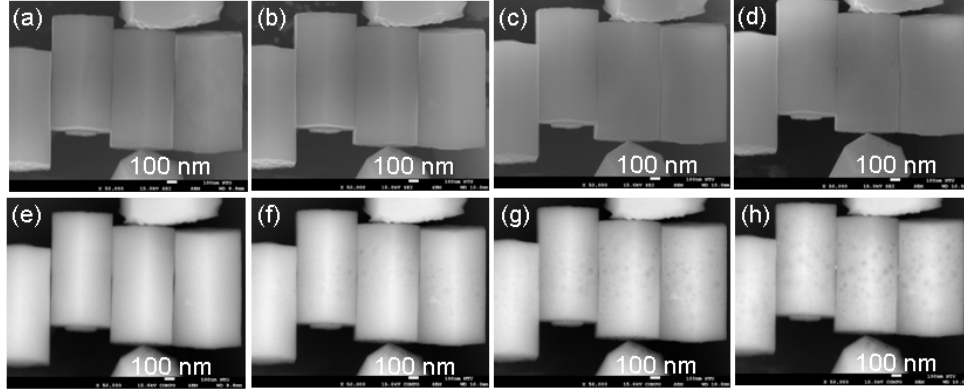


Fig. 5 (a): SEM image of four fallen un-doped ZnO NRs before thermal annealing. (b): SEM image of the sample in (a) after thermal annealing at 300 °C for 60 min with ambient oxygen. (c): SEM image of the sample in (b) after the second annealing process at 400 °C for 60 min with ambient oxygen. (d): SEM image of the sample in (c) after the third annealing process at 500 °C for 60 min with ambient oxygen. (e)-(h): BSEM images corresponding to the SEM images in parts (a)-(d), respectively.

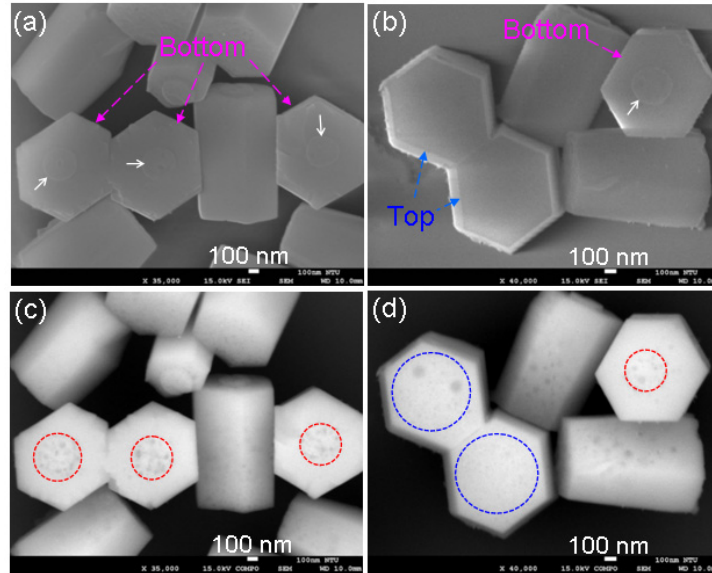


Fig. 6 (a) and (b): SEM images of a few fallen ZnO NRs showing either their bottom or top faces after the three-stage annealing process (the same condition as the sample in Fig. 5(d)). (c) and (d): The corresponding BSEM images of parts (a) and (b), respectively.



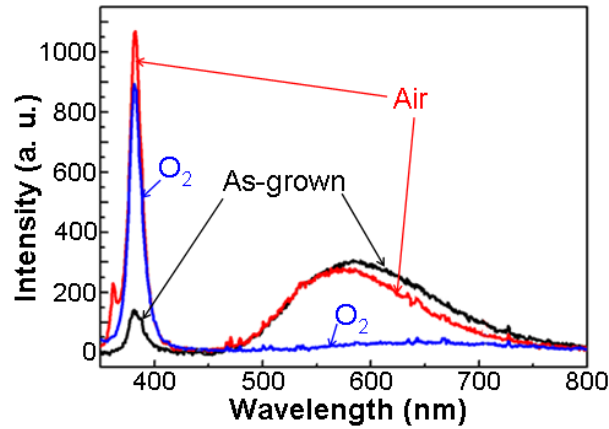


Fig. 7 PL spectra of un-doped ZnO NR array samples under the as-grown condition and the thermal annealing conditions of different ambient gases (air and oxygen). The NR array samples are grown with 0.08 M in solution concentration at 80 °C for 180 min. The thermal annealing conditions include 300 °C in temperature and 60 min in duration.

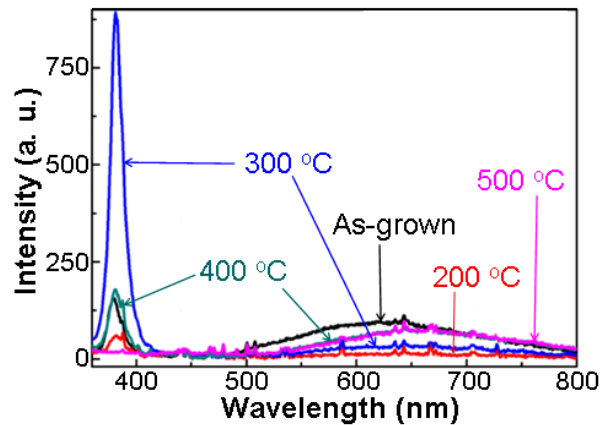


Fig. 8 PL spectra of Ga-doped ZnO NR array samples with different thermal annealing temperatures. The Ga-doped ZnO NRs are grown with 0.08 M in solution concentration and 0.003 M in doping concentration at 80 °C for 180 min. The annealing process is undertaken with ambient oxygen for 60 min.

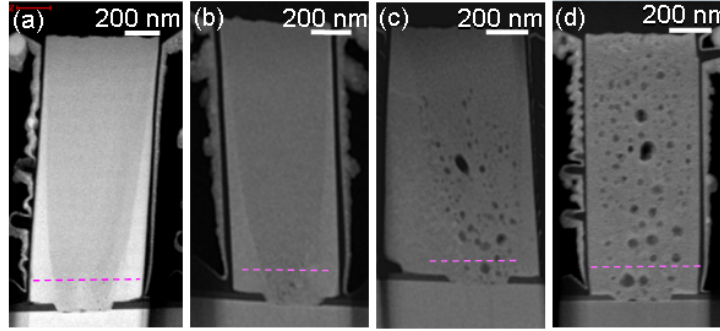


Fig. 9 (a): HAADF image of an as-grown Ga-doped NR sample. (b)-(d): HAADF images of the Ga-doped ZnO NR samples after they are thermally annealed at 200, 300, and 400 °C, respectively. The Ga-doped ZnO NRs are grown with 0.08 M in solution concentration and 0.003 M in doping concentration at 80 °C for 180 min. The annealing process is undertaken with ambient oxygen for 60 min. In each of those images, a horizontal dashed line is drawn, along which EDX analysis is made.

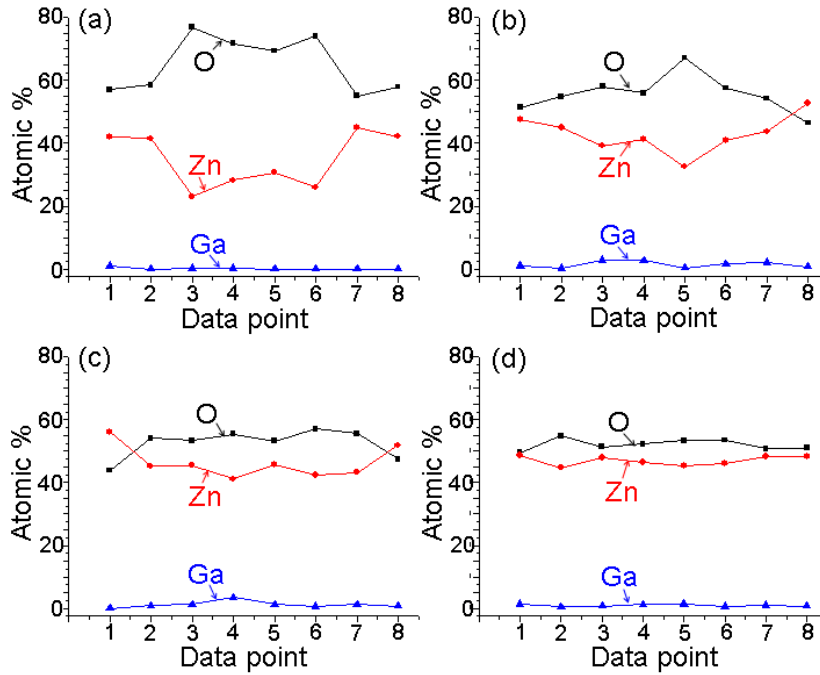


Fig. 10 (a)-(d): Atomic % levels of O, Zn, and Ga along the dashed lines in Figs. 9(a)-9(d), respectively. In each part, data points 1, 2, 7, and 8 (3-6) are located in the lateral- (vertical-) growth region.

### Part III:

#### Related Journal Publication List (acknowledging AOARD)

1. Chih-Yen Chen, Wen-Ming Chang, Wei-Lun Chung, Chieh Hsieh, Che-Hao Liao, Shao-Ying Ting, Kuan-Yu Chen, Yean-Woei Kiang, C. C. Yang, Wei-Siang Su, and Yung-Chen Cheng, "Crack-free GaN deposition on Si substrate with temperature-graded AlN buffer growth and the emission characteristics of overgrown InGaN/GaN quantum wells," to appear in Journal of Crystal Growth. (SCI)
2. Yang Kuo, Wen-Yen Chang, Horng-Shyang Chen, Yu-Renn Wu, C. C. Yang, and Yean-Woei Kiang, "Surface plasmon coupled emission enhancement of a quantum well with a metal nanoparticle embedded in a light-emitting diode," to appear in Journal of the Optical Society of America B-Optical Physics. (SCI)
3. Horng-Shyang Chen, Yu-Feng Yao, Che-Hao Liao, Charng-Gan Tu, Chia-Ying Su, Wen-Ming Chang, Yean-Woei Kiang, and C. C. Yang, "A Light-emitting Device with Regularly Patterned Growth of an InGaN/GaN Quantum-well Nanorod Light-emitting Diode Array," Optics Letters, Vol. 38, No. 18, September 15, 2013. (SCI)
4. Chun-Han Lin, Charng-Gan Tu, Horng-Shyang Chen, Chieh Hsieh, Chih-Yen Chen, Che-Hao Liao, Yean-Woei Kiang, and C. C. Yang, "Vertical light-emitting diodes with surface gratings and rough surfaces for effective light extraction," Optics Express, Vol. 21, No. 15, p. 17686~17694, 29 July 2013. (SCI)
5. Yang Kuo, Wen-Yen Chang, Horng-Shyang Chen, Yean-Woei Kiang, and C. C. Yang, "Surface plasmon coupling with a radiating dipole near an Ag nanoparticle embedded in GaN," Applied Physics Letters, Vol. 102, No. 16, p. 161103-1~4, 22 April 2013. (SCI)
6. Che-Hao Liao, Wen-Ming Chang, Yu-Feng Yao, Hao-Tsung Chen, Chia-Ying Su, Chih-Yen Chen, Chieh Hsieh, Horng-Shyang Chen, Charng-Gan Tu, Yean-Woei Kiang, C. C. Yang, and Ta-Cheng Hsu, "Cross-sectional sizes and emission wavelengths of regularly patterned GaN and core-shell InGaN/GaN quantum-well nanorod arrays," Journal of Applied Physics, Vol. 113, No. 5, p. 054315-1~9, 7 February 2013. (SCI)
7. Horng-Shyang Chen, Shao-Ying Ting, Che-Hao Liao, Chih-Yen Chen, Chieh Hsieh, Yu-Feng Yao, Hao-Tsung Chen, Yean-Woei Kiang, and C. C. Yang, "Vertical CdZnO/ZnO Quantum-well Light-emitting Diode," IEEE Photonics Technology Letters, Vol. 25, No. 3, p. 317~319, 1 February 2013. (SCI)
8. Horng-Shyang Chen, Chia-Phen Chen, Yang Kuo, Wang-Hsien Chou, Chen-Hung Shen, Yu-Lung Jung, Yean-Woei Kiang, and C. C. Yang, "Surface plasmon coupled light-emitting diode with metal protrusions into p-GaN," Applied Physics Letters, Vol. 102, No. 4, p. 041108-1~4, 28 January 2013. (SCI)
9. Ting-Ta Chi, Chiung-Ting Wu, Chen-Chin Liao, Yi-Chou Tu, Yean-Woei Kiang, and C. C. Yang, "Two-reference swept-source optical coherence tomography of high operation flexibility," Optics Express, Vol. 20, No. 27, p. 28418~28430, 17 December 2012. (SCI)
10. Chieh Hsieh, Horng-Shyang Chen, Che-Hao Liao, Chih-Yen Chen, Chun-Han Lin, Cheng-Hung Lin, Shao-Ying Ting, Yu-Feng Yao, Hao-Tsung Chen, Yean-Woei Kiang, and C. C. Yang, "Photoelectrochemical Liftoff of Patterned

- Sapphire Substrate for Fabricating Vertical Light-emitting Diode,” IEEE Photonics Technology Letters, Vol. 24, No. 19, p. 1775~1777, 1 October 2012. (SCI)
11. Shao-Ying Ting, Yu-Feng Yao, Wei-Lun Chung, Wen-Ming Chang, Chih-Yen Chen, Hao-Tsung Chen, Che-Hao Liao, Horng-Shyang Chen, Chieh Hsieh, and C. C. Yang, “Comparison of Emission Characteristics between the CdZnO/ZnO Quantum Wells on ZnO and GaN Templates,” Optics Express, Vol. 20, No. 20, p. 21860~21874, 24 September 2012. (SCI)
  12. Wen-Ming Chang, Che-Hao Liao, Chih-Yen Chen, Chieh Hsieh, Tsung-Yi Tang, Yean-Woei Kiang, and C. C. Yang, “Spiral deposition with alternating indium composition in growing an InGaN nano-needle with the vapor-liquid-solid growth mode,” Journal of Nanomaterials, Vol. 2012, Article ID 653195, 7 pages, 5 July 2012. (SCI)
  13. Che-Hao Liao, Wen-Ming Chang, Horng-Shyang Chen, Chih-Yen Chen, Yu-Feng Yao, Hao-Tsung Chen, Chia-Ying Su, Shao-Ying Ting, Yean-Woei Kiang, and C. C. Yang, “Geometry and composition comparisons between c-plane disc-like and m-plane core-shell InGaN/GaN quantum wells in a nitride nanorod,” Optics Express, Vol. 20, No. 14, p. 15859~15871, 2 July 2012. (SCI)
  14. Shao-Ying Ting, Horng-Shyang Chen, Wen-Ming Chang, Jeng-Jie Huang, Che-Hao Liao, Chih-Yen Chen, Chieh Hsieh, Yu-Feng Yao, Hao-Tsung Chen, Yean-Woei Kiang, and C. C. Yang, “MBE-grown CdZnO/ZnO Multiple Quantum-well Light-emitting Diode on MOCVD-grown p-type GaN,” IEEE Photonics Technology Letters, Vol. 24, No. 11, p. 909~911, 1 June 2012. (SCI)